

THE PROPERTIES OF H α EMISSION-LINE GALAXIES AT Z = 2.24[†]

FANG XIA AN¹, XIAN ZHONG ZHENG¹, WEI-HAO WANG², JIA-SHENG HUANG^{3,4}, XU KONG⁵, JUN-XIAN WANG⁵, GUAN WEN FANG^{6,7}, FEIFAN ZHU⁵, QIU-SHENG GU⁸, HONG WU⁴, LEI HAO⁹, AND XIAO-YANG XIA¹⁰

Published online: 2014 March 18

ABSTRACT

Using deep narrow-band H_2S1 and K_s -band imaging data obtained with CFHT/WIRCam, we identify a sample of 56 H α emission-line galaxies (ELGs) at $z = 2.24$ with the 5σ depths of $H_2S1 = 22.8$ and $K_s = 24.8$ (AB) over 383 arcmin^2 area in the Extended Chandra Deep Field South. A detailed analysis is carried out with existing multi-wavelength data in this field. Three of the 56 H α ELGs are detected in *Chandra* 4 Ms X-ray observations and two of them are classified as active galactic nuclei. The rest-frame UV and optical morphologies revealed by *HST*/ACS and WFC3 deep images show that nearly half of the H α ELGs are either merging systems or have a close companion, indicating that the merging/interacting processes play a key role in regulating star formation at cosmic epoch $z = 2-3$; About 14% are too faint to be resolved in the rest-frame UV morphology due to high dust extinction. We estimate dust extinction from spectral energy distributions. We find that dust extinction is generally correlated with H α luminosity and stellar mass. Our results suggest that H α ELGs are representative of star-forming galaxies. Applying extinction corrections for individual objects, we examine the intrinsic H α luminosity function (LF) at $z = 2.24$, obtaining a best-fit Schechter function characterized by a faint-end slope of $\alpha = -1.3$. This is shallower than the typical slope of $\alpha = \sim -1.6$ in previous works based on constant extinction correction. We demonstrate that this difference is mainly due to the different extinction corrections. The proper extinction correction is thus the key to recovering the intrinsic LF as the extinction globally increases with H α luminosity. Moreover, we find that our H α LF mirrors the stellar mass function of star-forming galaxies at the same cosmic epoch. This finding indeed reflects the tight correlation between star formation rate and stellar mass for the star-forming galaxies, i.e., the so-called main sequence.

Subject headings: galaxies: evolution - galaxies: high-redshift - galaxies: luminosity function, mass function - galaxies: star formation

1. INTRODUCTION

The cosmic star formation rate (SFR) density peaks at $z \sim 2-3$ and rapidly declines to the present day (Hopkins & Beacom 2006; Karim et al. 2011; Sobral et al. 2013, and references therein). Systematic studies of galaxy populations at the peak epoch hold the key to our understanding of galaxy formation and evolution, in particular for massive galaxies. The population of massive quiescent galaxies began to emerge

(e.g., Brammer et al. 2011) and the bulk of stars in local massive galaxies were formed at $z > \sim 1.5$ (Renzini 2006). A number of techniques have been developed to probe different galaxy populations in this crucial epoch, including Lyman break selection (Steidel et al. 1999), red color cut (Franx et al. 2003), BzK selection (Daddi et al. 2004), submillimeter detection (Chapman et al. 2005) and narrow-band imaging (Moorwood et al. 2000; see Shapley 2011 for a review). A complete picture is still missing due to the short of spectroscopic follow ups in the “redshift desert” $1.4 < z < 2.5$ for large samples selected in terms of physical quantities such as stellar mass or SFR.

The deep near-infrared (NIR) observations play a central role in probing high- z galaxies in the rest-frame optical, which is more reflective of older stars (hence stellar mass). The NIR narrow-band imaging has turned out to be a modest way to identify emission-line galaxies (ELGs) in a narrow redshift range ($\delta z/(1+z) = 1\% - 2\%$) over large sky coverage (Sobral et al. 2013). It provides redshifts with higher precision than the photometric redshift method based on broad-band spectral energy distributions (SEDs), and allows us to distinguish environments (e.g., groups or clusters) traced by the ELGs (e.g., Matsuda et al. 2011; Hatch et al. 2011; Geach et al. 2012). Moreover, the strength of an emission line, such as H α and [O II] $\lambda 3727$, can be measured by the flux excess in the narrow-band with respect to the corresponding broad-band. The optical and NIR emission lines from ionized gas surrounding massive young stars represent a nearly instantaneous measure of the SFR (Kennicutt & Evans 2012). The H α is often used as an SFR indicator because it is the strongest emission line in the optical/NIR, and less affected by dust obscuration com-

¹ Purple Mountain Observatory, China Academy of Sciences, West Beijing Road 2, Nanjing 210008, China; fangxiaan@pmo.ac.cn

² Academia Sinica Institute of Astronomy and Astrophysics, Taipei 10617, Taiwan

³ Harvard-Smithsonian Center for Astrophysics, 60 Garden Street, Cambridge, MA 02138, USA

⁴ National Astronomical Observatories, Chinese Academy of Sciences, Beijing 100012, China

⁵ CAS Key Laboratory for Research in Galaxies and Cosmology, Department of Astronomy, University of Science and Technology of China, Hefei 230026, China

⁶ Institute for Astronomy and History of Science and Technology, Dali University, Yunnan 671003, China

⁷ Key Laboratory of Modern Astronomy and Astrophysics, Nanjing University, Ministry of Education, Nanjing 210093, China

⁸ School of Astronomy and Space Science, Nanjing University, 22 Hankou RD, Nanjing 210093, China

⁹ Shanghai Astronomical Observatory, Chinese Academy of Sciences, 80 Nandan Road, Shanghai 2000 30, China

¹⁰ Tianjin Astrophysics Center, Tianjin Normal University, Tianjin 300387, China

[†] Based on observations obtained with WIRCam, a joint project of CFHT, Taiwan, Korea, Canada, France, and the Canada-France-Hawaii Telescope (CFHT) which is operated by the National Research Council (NRC) of Canada, the Institut National des Sciences de l’Univers of the Centre National de la Recherche Scientifique of France, and the University of Hawaii.

pared to emission lines in the UV such as Ly α in typical star-forming galaxies (SFGs).

The past decade has seen a number of NIR narrow-band surveys using ground-based telescopes (e.g., Geach et al. 2008; Ly et al. 2011) and NIR grism spectroscopic surveys with the *Hubble Space Telescope* (*HST*; e.g., Yan et al. 1999; Atek et al. 2010; van Dokkum et al. 2011; Colbert et al. 2013) in the study of H α ELGs at $z > 0.4$, yielding H α luminosity functions (LFs) with a steep faint-end slope $\alpha \sim -1.6$ out to $z \sim 2.5$ (Hayes et al. 2010; Ly et al. 2011; Sobral et al. 2013). The derived H α LFs suffer from large uncertainties mostly arising from poor extinction correction due to the lack of ancillary data. Detailed studies of the properties of H α ELGs will help to reduce the uncertainties. On the other hand, SFGs are found to follow a tight correlation between SFR and stellar mass (e.g., Noeske et al. 2007; Daddi et al. 2007). This correlation, namely the main sequence, has been convincingly established from the local universe (Brinchmann et al. 2004) to high-redshift universe (Guo et al. 2013; Peng et al. 2010; Karim et al. 2011; Reddy et al. 2012). One would expect that the SFR function traces the stellar mass function (SMF) for SFGs. Since H α luminosity is a direct measure of SFR, the H α LF is expected to mirror the SMF. However, the SMF tends to have a shallow faint-end with a slope $\alpha \sim -1.3$ over a wide redshift range $0 < z < 3$ (e.g., Ilbert et al. 2010; Brammer et al. 2011). The cause of this discrepancy in the faint-end slope between the two functions remains to be explored.

We carry out a deep 2.13 μm narrow-band imaging survey to search for H α ELGs at $z = 2.24$ in the Extended Chandra Deep Field South (ECDFS). This field contains the deepest observations from *Chandra*, *Galaxy Evolution Explorer*, *HST*, and *Spitzer*. With these data, we are able to securely identify a sample of H α ELGs, perform a detailed analysis and determine the intrinsic H α LF. We show that resolving dusty SFGs with intrinsically luminous H α from those with observed faint H α leads to a shallow faint-end slope for the H α LF. We describe observations and data reduction in Section 2. Section 3 gives the selection of H α ELGs and SED analysis to obtain photometric redshift, stellar mass and extinction. We present the properties of H α ELGs in Section 4. The derived H α LF at $z = 2.24$ is given in Section 5. We discuss and summarize our results in Section 6. Throughout the paper we adopt a cosmology with $[\Omega_\Lambda, \Omega_M, h_{70}] = [0.7, 0.3, 1.0]$. Kroupa initial mass function (IMF; Kroupa 2001) and the AB magnitude system (Oke 1974) are used unless otherwise stated.

2. OBSERVATIONS AND DATA REDUCTION

The deep narrow-band imaging of the ECDFS ($\alpha = 03:28:45$, $\delta = -27:48:00$) were taken with WIRCam on board the Canada-France-Hawaii Telescope (CFHT; Puget et al. 2004) through the H_2S1 filter ($\lambda_c = 2.130 \mu\text{m}$, $\Delta\lambda = 0.0293 \mu\text{m}$). WIRCam is equipped with four 2048 \times 2048 HAWAII2-RG detectors, providing a field of view $20' \times 20'$ and a pixel scale of $0''.3 \text{ pixel}^{-1}$. The gaps between detectors are $45''$. The H_2S1 observations were carried out under seeing conditions of $0''.6\text{--}0''.8$ with a total integration time of 17.22 hrs in semester 2011B. Dithering technique was adopted in observations in order to remove bad pixels and cover gaps between detectors.

The data were reduced using the pipeline *SIMPLE* (Simple Imaging and Mosaicking Pipeline) written in IDL (Wang et al. 2010; Hsieh et al. 2012), which include flat-fielding, background subtraction, removing cosmic rays, and instrumental features like crosstalk and residual images from saturated ob-

jects in previous exposures and masking satellite trails. Because of the rapid variation of sky background in the NIR, only exposures taken in the same dithering block (within 40 minutes) and by the same detector are reduced in the same run and combined into a background-subtracted science image. After that, the science images of four detectors are mosaicked into a frame science image. The H_2S1 images are astrometrically calibrated with the *HST* observations from the Galaxy Evolution from Morphology and SEDs (GEMS; Rix et al. 2004; Caldwell et al. 2008) survey using a list of 7415 compact sources with $K_s < 21.5$. The accuracy of astrometry is $\sim 0''.1$. The final science image was produced by co-adding 326 frame science images. The exposure time map was also created in the co-adding. The photometric calibration is performed with the K_s -band photometric catalog of the Great Observatories Origins Deep Survey (GOODS) South extracted from VLT/ISAAC observations (Retzlaff et al. 2010). In total 125 point sources with $16.0 < K_s < 19.0$ are chosen as photometric standard stars used to build empirical point spread function (PSF). A correction of 1.26 is derived from the empirical PSF to convert a flux integrated within an aperture of diameter of $2''$ into the total flux. The calibrated fluxes of the chosen point sources in our mosaic H_2S1 image only show 1% scatter compared with these given in the reference catalog. The final H_2S1 science image has 383 arcmin 2 area with a total integrated exposure time > 10 hr (and > 15 hr for 47.3%). We limited source detection in this area, where a 5σ depth corresponds to 22.8 mag for point sources.

We also utilize K_s -band ($\lambda_c = 2.146 \mu\text{m}$, $\Delta\lambda = 0.325 \mu\text{m}$) imaging of ECDFS obtained with CFHT/WIRCam (Hsieh et al. 2012). The K_s -band observations were taken with CFHT/WIRCam in semesters 2009B and 2010B. The data were reduced and calibrated in the same way as we describe above for the H_2S1 data. The K_s image reaches a 5σ depth of $K_s = 24.8$ mag for point sources in the H_2S1 source detection region. More technical details can be found in Wang et al. (2010) and Hsieh et al. (2012). The 5σ limit for extended sources with a Sérsic index of unity is 0.4 mag lower for the H_2S1 image and 0.3 mag lower for the K_s image.

3. SAMPLE SELECTION

3.1. Selection of Emission-line Objects

We use SExtractor software (Bertin & Arnouts 1996) to detect sources and measure fluxes in the H_2S1 image. A minimum of five contiguous pixels with fluxes $> 2.5\sigma$ of the background noise is required for a secure source detection. The exposure map is taken as weight image to reduce spurious detections in low signal-to-noise (S/N) regions. The “dual-image” mode in SExtractor is used to perform photometry in the K_s image, namely, to measure fluxes in the K_s image over the same area of a detection as in the H_2S1 image. Of course, the two images are well aligned into the same frame. In total, 8720 sources are securely detected with an $S/N > 5$ in both images.

As we have stated in Section 1, the narrow-band excess is an emission-line indicator that is widely used to identify emission-line objects. Here we use $K_s - H_2S1$ to probe H α emission-line objects following Bunker et al. (1995). A secure and significant narrow-band excess is mainly determined by the background noises of the narrow- and broad-band images σ_{H_2S1} and σ_{K_s} as follows:

$$K_s - H_2S1 > \Sigma \sqrt{\sigma_{K_s}^2 + \sigma_{H_2S1}^2}, \quad (1)$$

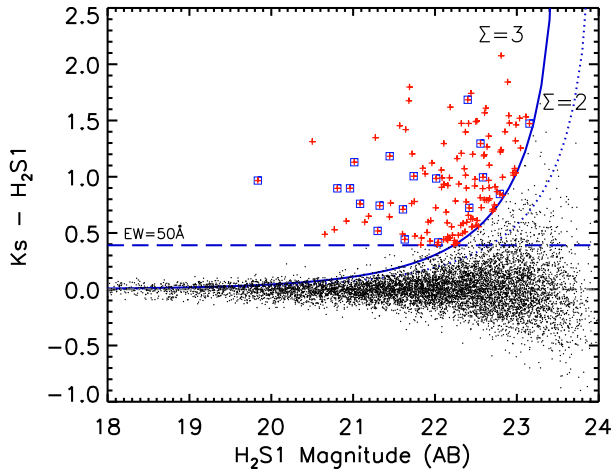


FIG. 1.— Color-magnitude diagram for H_2S1 detected objects. The blue solid/dotted line represents the limitation due to background noise at the $\Sigma = 3/\Sigma = 2$ level. The blue dashed line marks the excess cut corresponding to the rest-frame $EW = 50 \text{ \AA}$. The red crosses are the 140 emission-line candidates. The blue squares mark the candidates with spec- z .

where the right-hand side term is the combined background noise of the two bands and Σ is the significant factor. Figure 1 shows the $K_s - H_2S1$ color as a function of H_2S1 magnitude for 8720 sources. The solid curve represents the combined noise with $\Sigma = 3$ and the dotted curve refers to the noise with $\Sigma = 2$. We adopt $\Sigma > 3$ to select emission-line candidates. In order to minimize false excess caused by photon noises of bright objects, we also employ an empirical cut $EW > 50 \text{ \AA}$ following Geach et al. (2008), where EW refers to the rest-frame equivalent width of an emission line. This cut corresponds to $K_s - H_2S1 > 0.39$ mag. We note that a lower EW cut (e.g., $EW > 30 \text{ \AA}$) only increases a few more candidates and will not significantly change on our results.

As shown in Figure 1, 146 emission-line candidates are selected with $\Sigma > 3$ and $EW > 50 \text{ \AA}$. To examine how many spurious sources will be selected by our criteria, we perform a “negative” selection with $K_s - H_2S1 < -0.39$ mag and -3Σ cut. Only one object being selected means our criteria enable a clean selection of emission-line object candidates. Furthermore, we perform a visual examination of our selected candidates. Of the 146, six are visually identified as spurious sources like spikes of bright stars or contaminations that were not rejected by data reduction. The other 140 candidates are expected to be objects with a strong emission line between $\text{Pa}\alpha$ at $z = 0.14$ and $\text{Ly}\alpha$ at $z = 16.52$. And 33 of the 140 objects are found to have spectroscopic redshifts from the catalog collected by Cardamone et al. (2010).

It is worth noting that the requirement of a secure detection ($> 5\sigma$) in the K_s might miss emission-line objects with very high EW s. To quantify this effect, we re-examine H_2S1 sources and find 14 objects with $K_s \geq 24.8$ mag. Among them, six are visually identified as spurious sources. The other eight sources are very faint ($H_2S1 > 22.5$ mag), compared to the detection limit of $H_2S1 = 22.8$ mag. We suspect that their very high EW s ($> 500 \text{ \AA}$) would be dominated by noise and the intrinsic EW s could be lower. Considering that H α emitters represent 30%–40% of all emitters (Hayes et al. 2010; Lee et al. 2012), less than three of the eight sources are expected to be H α emitters. Moreover, they must be very low-mass galaxies with given K_s magnitudes. The missing fraction of

H α emitters with very high EW s is estimated to be very small ($< 5\%$). We therefore conclude that inclusion of the selection criterion $K_s < 24.8$ mag has negligible detrimental effects on our main results.

3.2. Photometric Redshifts and SED Modeling

To measure fluxes and construct SEDs for the selected 140 emission-line objects, we use 12 bands imaging data, including U , B , V , R and I -band data from the Multiwavelength Survey by Yale-Chile (MUSYC; Gawiser et al. 2006), HST/ACS F606W (V_{606}) and F850LP (z_{850}) imaging from GEMS (Rix et al. 2004; Caldwell et al. 2008), $HST/WFC3$ F125W (J_{125}) and F160W (H_{160}) imaging from the Cosmic Assembly Near-infrared Deep Extragalactic Legacy Survey (CANDELS; Grogin et al. 2011; Koekemoer et al. 2011), and CFHT/WIRCam J and K_s imaging (Hsieh et al. 2012) in combination with our H_2S1 data. Only 72 of the 140 have J_{125} and H_{160} data because CANDELS observations only cover the central part of ECDFS, i.e. the GOODS-South region. The 12 bands images have distinct PSFs. The HST images have PSFs with FWHM $\sim 0''.1 - 0''.16$, compared to $\sim 1''$ for the MUSYC images and $\sim 0''.8$ for the CFHT images.¹²

Instead of measuring fluxes within the same aperture from the 12 bands images downgraded to the worst PSF, we intend to maximize S/N for aperture-matched colors between the 12 bands. We first determine colors for MUSYC, HST and CFHT bands, respectively. Second, we match three sets of colors to establish SEDs from the U to the K_s . The aperture-matched fluxes in the U , B , V , R and I (and thus colors between them) are available for 124 of the 140 targets from the MUSYC public catalog (Cardamone et al. 2010). The other 16 are optically too faint to be detected by MUSYC observations. For the HST data set, V_{606} and z_{850} images are convolved with H_{160} PSF, while J_{125} and H_{160} images are convolved with z_{850} PSF. These operations enable us to match the four images to the same spatial resolution. An aperture of diameter of $1''$ is used to measure fluxes from the convolved images and give aperture-matched colors between the four HST bands. Colors between CFHT J , K_s and H_2S1 bands are derived from photometry over the same area of a target using SExtractor in “dual-image” mode. The next step is to match MUSYC, HST and CFHT colors to the same aperture. This is done by deriving the aperture-matched color between the J_{125} (z_{850} instead if J_{125} is not available) and J bands, and that between the V_{606} and V bands. Since J_{125}/z_{850} -band PSF ($0''.13/0''.1$) is much smaller than J -band PSF ($0''.8$), we convolve the J_{125}/z_{850} image with the J -band PSF to match the spatial resolution of J -band image. An aperture of $2''$ diameter is used to measure fluxes accordingly. Moreover, the MUSYC colors are linked to the HST -band colors by matching the interpolated V_{606} between V - and R -band magnitudes with V_{606} . The aperture-matched colors establish the $U - K_s$ SED. The SED is then scaled up to meet the total magnitude of K_s derived from aperture photometry within a diameter of $2''$ corrected for missing flux out of the aperture (see Retzlaff et al. 2010 for more details). By doing so, we obtain SEDs for our 140 emission-line objects.

The software tool EAZY (Easy and Accurate Redshifts from Yale; Brammer et al. 2008) is used to derive photometric redshifts (photo- z). The template-fitting method used in EAZY to estimate photo- z suffers from the fact that template color frequently degenerates with redshift. The K_s mag-

¹² See An et al. (2013) for a summary of these data.

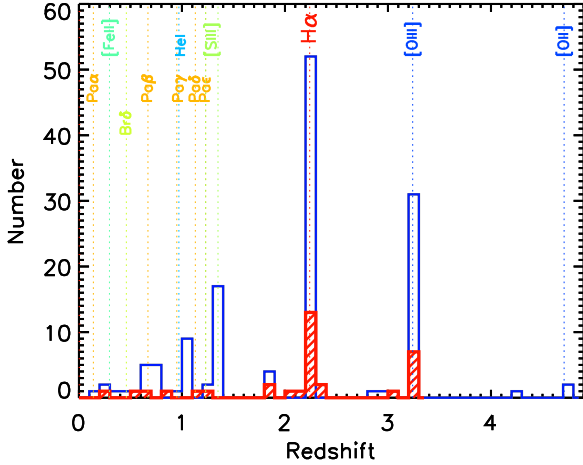


FIG. 2.— Distribution of photo- z for 138 selected emission-line candidates. The red shaded area shows the distribution of 33 candidates with spec- z . The dotted lines mark the emission-lines detected by the H_2S1 filter at given redshifts.

nitude is then taken as a Bayesian prior to assigning a low probability to a very low redshift and a similarly low probability for finding extremely bright galaxies at high- z . The emission-line objects selected with NIR narrow-band excess are mostly, if not all, SFGs (e.g., see Hayes et al. 2010). Therefore, the default library of galaxy templates in EAZY is chosen to derive photo- z . The library includes five templates generated based on the PÉGASe population synthesis models (Fiac & Rocca-Volmerang 1997) and calibrated with synthetic photometry from semi-analytic models, and one template of young ($t = 50$ Myr) and dusty ($A_V = 2.75$) starbursts. The combination of the six templates is able to model galaxies with colors over a broad range and minimize the color and redshift degeneracy. Moreover, the PÉGASe models provide a self-consistent treatment of emission lines. Among 140 emission-line objects, two have SED composed of < 5 valid data points and fail to produce photo- z .

Figure 2 shows the distribution of photo- z for the 138 objects. The 33 objects with spec- z are shown by the hatched regions. The emission lines potentially detected by H_2S1 are marked. We can clearly see two prominent peaks at $z \sim 2.24$ and $z \sim 3.25$, corresponding to the emission lines $H\alpha$ and $[O III]$, respectively. These two peaks are confirmed by the spec- z distribution. The good agreement between spec- z and our photo- z indicates that our H_2S1 data are critical to determining photo- z to a relatively-high precision. Other two peaks at $z \sim 1.3$ and $z \sim 1.0$ contain 17 and 10 objects, respectively. The peak at $z \sim 1.3$ corresponds to $[S III]\lambda 9096$, while the peak at $z \sim 1.0$ corresponds to $P\gamma\lambda 10935$, $P\delta\lambda 10047$ or $He I\lambda 10830$ lines. The relatively high abundance of $[S III]\lambda 9096$ was seldom reported in the literature. We further examine their properties in An et al. (2013). We note that two objects have photo- z corresponding to no known strong emission lines. They are located close to the $\Sigma = 3$ line in Figure 1. We argue that the two objects are likely noise contaminants.

Accounting for potential uncertainties in photo- z (see also Lee et al. 2012), we take 56 objects with $1.8 < z_{\text{phot}} < 2.6$ as $H\alpha$ emitters at $z = 2.24$. Similarly, we identify 34 $[O III]$ emitters at $z = 3.25$, two $[O II]$ emitters at $z = 6.72$, and other emitters at lower redshifts, including $Pa\alpha$ at $z = 0.14$, $[Fe II]$

at $z = 0.30$ and $[S III]$ at $z = 1.23/1.35$. Here the percentage of $H\alpha$ emitters among all emitters is 40% (56/140), consistent with $\sim 36\%$ in Hayes et al. (2010) and Lee et al. (2012). We show the best-fit SED models and the probability function of photo- z for the 56 $H\alpha$ emitters in Figure 3. Table 1 lists their multi-band photometry and Table 2 gives their photo- z and spec- z .

4. PROPERTIES OF $H\alpha$ EMISSION-LINE GALAXIES

4.1. X-Ray Properties

We first match our $H\alpha$ emitters with the X-ray source catalog of 4 Ms *Chandra* exposure in CDFS (Xue et al. 2011) to examine their X-ray properties. Three out of 56 $H\alpha$ emitters are detected in X-ray (X-ray source ID = 29, 399, and 435 in the *Chandra* catalog), with absorption-corrected rest-frame 0.5-8 keV luminosities 2.60×10^{43} , 2.76×10^{42} , and 1.15×10^{43} erg s $^{-1}$, respectively. While the faintest X-ray among the three (X-ray source ID = 399) was identified as a galaxy, the other two more luminous X-ray sources were classified as active galactic nuclei (AGNs), both of which are likely obscured AGNs according to their X-ray hardness ratios (Xue et al. 2011). In addition, we find that the three $H\alpha$ sources have luminosity $L_{H\alpha} > 10^{43.5}$ erg s $^{-1}$, being the most luminous ones in our sample and also the most massive ones with $M > 10^{11} M_{\odot}$ (see Section 4.5).

For the other non-detected X-ray $H\alpha$ emitters, we perform X-ray stacking analyses using 4 Ms *Chandra* exposures. We exclude sources with no X-ray coverage or with contaminations from nearby bright X-ray sources. We finally stacked X-ray images of 42 $H\alpha$ emitters, yielding an effective exposure time of 106 Ms. We find a marginal detection in the stacked 0.5-2 keV image ($S/N = 2.5$), and obtain an average rest frame 0.5-2.0 keV X-ray luminosity of $3.5 \pm 1.4 \times 10^{42}$ erg s $^{-1}$ by assuming a power-law spectrum with photon index of 2.0. This confirms that the vast majority of our sample consists of star-forming ones.

4.2. Morphologies

HST/ACS V_{606} and z_{850} imaging data are used to examine morphologies. The two bands correspond to the rest-frame 1839Å and 2794Å for $z = 2.24$. *HST/WFC3* imaging data from CANDELS are available for 26 of our 56 sample targets.

Figure 4 shows *HST* $V_{606}+z_{850}$ color image stamps for 55 $H\alpha$ ELGs and $J_{125}+H_{160}$ color image stamp for one (the third from the top and third from the left). One can see that the $H\alpha$ ELGs in our sample show a variety of morphologies. The 56 $H\alpha$ ELGs are visually classified by three of us (X. Z. Z., F. X. A and G. W. F) and the median types are given in Table 2. About 20% (11/56) of the sample galaxies contain two major components of similar color and are separated by $\sim 1'' - 2''$ (8 – 17 kpc), which eliminates the possibility of them being multiple clumps within a single galaxy; 25% (14/56) appear to be merger remnants with tails, ‘tadpole’, or a peculiar shape; 23% (13/56) show spiral/diffuse/clumpy morphologies; 18% (10/56) are compact; 14% (8/56) are too faint to be resolved ($V_{606} < 26$). We point out that the V_{606}/z_{850} -faint $H\alpha$ galaxies are indeed dusty starbursts and their rest-frame UV lights are heavily attenuated. The UV-selection (e.g., Lyman break technique) is unable to pick up such dusty SFGs. This also suggests that the dust extinction of SFGs varies in a wide range. Of three X-ray sources, two are found in merging systems and one is a compact galaxy.

TABLE 1
MULTI-BAND PHOTOMETRY OF OUR SAMPLE OF H α ELGS

ID	Mag_U	Mag_B	Mag_V	Mag_V ₆₀₆	Mag_R	Mag_J	Mag_8500	Mag_J ₁₂₅	Mag_J	Mag_H160	Mag_Ks	Mag_H β ST	Mag_24 μ m
1	25.62 \pm 0.18	24.56 \pm 0.02	24.34 \pm 0.03	24.28 \pm 0.02	24.23 \pm 0.02	24.41 \pm 0.15	24.16 \pm 0.03	23.76 \pm 0.02	23.69 \pm 0.05	23.17 \pm 0.01	23.11 \pm 0.04	21.89 \pm 0.05	-99.99
2	-99.99 ^a	25.29 \pm 0.06	24.93 \pm 0.06	24.72 \pm 0.03	24.52 \pm 0.04	24.29 \pm 0.18	23.94 \pm 0.03	22.92 \pm 0.01	22.96 \pm 0.03	22.24 \pm 0.01	21.72 \pm 0.02	21.18 \pm 0.04	18.39 \pm 0.21
3	-99.99	25.32 \pm 0.05	25.15 \pm 0.06	25.06 \pm 0.02	24.98 \pm 0.04	-99.99	24.68 \pm 0.03	24.22 \pm 0.02	24.09 \pm 0.06	23.73 \pm 0.02	23.28 \pm 0.04	22.43 \pm 0.07	-99.99
4	-99.99	25.90 \pm 0.11	25.84 \pm 0.05	25.79 \pm 0.09	25.79 \pm 0.09	-99.99	25.40 \pm 0.07	24.85 \pm 0.04	24.65 \pm 0.11	24.16 \pm 0.02	23.65 \pm 0.07	22.84 \pm 0.12	-99.99
5	24.17 \pm 0.03	23.45 \pm 0.01	23.37 \pm 0.01	23.37 \pm 0.01	23.37 \pm 0.01	23.31 \pm 0.06	23.38 \pm 0.01	23.26 \pm 0.01	23.21 \pm 0.03	22.73 \pm 0.01	22.77 \pm 0.03	21.86 \pm 0.05	-99.99
6	-99.99	25.19 \pm 0.03	25.19 \pm 0.03	25.19 \pm 0.03	25.19 \pm 0.03	25.19 \pm 0.03	26.25 \pm 0.17	24.62 \pm 0.03	24.51 \pm 0.10	23.90 \pm 0.02	24.20 \pm 0.12	22.80 \pm 0.12	-99.99
7	25.34 \pm 0.08	24.75 \pm 0.03	24.69 \pm 0.04	24.65 \pm 0.02	24.60 \pm 0.03	24.19 \pm 0.13	24.34 \pm 0.03	23.76 \pm 0.01	23.79 \pm 0.04	23.32 \pm 0.01	23.32 \pm 0.05	22.63 \pm 0.11	-99.99
8	26.34 \pm 0.18	25.39 \pm 0.05	25.14 \pm 0.05	25.09 \pm 0.02	25.04 \pm 0.05	24.96 \pm 0.24	24.55 \pm 0.03	23.86 \pm 0.01	23.80 \pm 0.04	23.45 \pm 0.01	22.89 \pm 0.03	22.53 \pm 0.09	-99.99
9	25.68 \pm 0.12	24.23 \pm 0.02	23.94 \pm 0.02	23.92 \pm 0.01	23.90 \pm 0.02	23.60 \pm 0.10	23.40 \pm 0.01	22.72 \pm 0.01	22.66 \pm 0.02	22.30 \pm 0.01	21.79 \pm 0.02	21.09 \pm 0.04	19.41 \pm 0.32
10	25.55 \pm 0.08	24.83 \pm 0.03	24.74 \pm 0.03	24.78 \pm 0.02	24.82 \pm 0.04	24.78 \pm 0.19	24.71 \pm 0.03	24.53 \pm 0.02	24.38 \pm 0.08	24.10 \pm 0.02	24.14 \pm 0.11	22.74 \pm 0.11	-99.99
11	25.79 \pm 0.23	24.78 \pm 0.03	24.62 \pm 0.03	24.64 \pm 0.02	24.65 \pm 0.03	24.61 \pm 0.19	24.58 \pm 0.03	24.37 \pm 0.02	24.13 \pm 0.06	23.77 \pm 0.01	23.65 \pm 0.07	22.50 \pm 0.09	-99.99
12	25.45 \pm 0.09	24.50 \pm 0.02	24.31 \pm 0.03	24.34 \pm 0.01	24.34 \pm 0.02	24.33 \pm 0.15	24.21 \pm 0.02	23.70 \pm 0.01	23.56 \pm 0.04	23.40 \pm 0.01	23.06 \pm 0.04	22.41 \pm 0.08	-99.99
13	25.21 \pm 0.07	24.42 \pm 0.02	24.42 \pm 0.03	24.45 \pm 0.01	24.48 \pm 0.03	24.46 \pm 0.16	24.53 \pm 0.03	24.55 \pm 0.02	24.58 \pm 0.08	23.88 \pm 0.01	23.83 \pm 0.08	22.23 \pm 0.07	-99.99
14	-99.99	25.95 \pm 0.09	25.81 \pm 0.10	25.77 \pm 0.04	25.74 \pm 0.09	-99.99	25.67 \pm 0.08	25.21 \pm 0.04	25.06 \pm 0.13	24.37 \pm 0.02	24.80 \pm 0.18	22.99 \pm 0.13	-99.99
15*	24.60 \pm 0.20	23.57 \pm 0.01	23.40 \pm 0.01	23.36 \pm 0.01	23.33 \pm 0.01	23.18 \pm 0.07	23.06 \pm 0.01	22.54 \pm 0.00	22.60 \pm 0.02	22.17 \pm 0.00	21.68 \pm 0.02	20.83 \pm 0.03	18.59 \pm 0.23
16*	25.05 \pm 0.08	23.96 \pm 0.02	23.64 \pm 0.02	23.46 \pm 0.01	23.28 \pm 0.01	22.88 \pm 0.05	22.68 \pm 0.01	21.91 \pm 0.00	21.88 \pm 0.01	21.29 \pm 0.00	20.73 \pm 0.01	19.81 \pm 0.01	17.82 \pm 0.16
17	24.77 \pm 0.06	24.11 \pm 0.02	23.85 \pm 0.02	23.85 \pm 0.02	23.74 \pm 0.02	23.60 \pm 0.11	23.37 \pm 0.01	23.37 \pm 0.01	22.94 \pm 0.03	22.82 \pm 0.01	22.41 \pm 0.03	21.10 \pm 0.03	19.67 \pm 0.35
18	-99.99	25.86 \pm 0.15	24.85 \pm 0.04	24.80 \pm 0.02	24.36 \pm 0.03	24.06 \pm 0.15	23.85 \pm 0.03	23.02 \pm 0.01	22.91 \pm 0.03	22.49 \pm 0.01	21.94 \pm 0.02	21.24 \pm 0.04	19.05 \pm 0.28
19	-99.99	25.86 \pm 0.15	24.85 \pm 0.04	24.80 \pm 0.02	24.36 \pm 0.03	24.06 \pm 0.15	23.85 \pm 0.03	23.02 \pm 0.01	22.91 \pm 0.03	22.49 \pm 0.01	21.94 \pm 0.02	21.24 \pm 0.04	19.05 \pm 0.28
20	-99.99	25.86 \pm 0.15	24.85 \pm 0.04	24.80 \pm 0.02	24.36 \pm 0.03	24.06 \pm 0.15	23.85 \pm 0.03	23.02 \pm 0.01	22.91 \pm 0.03	22.49 \pm 0.01	21.94 \pm 0.02	21.24 \pm 0.04	19.05 \pm 0.28
21	25.83 \pm 0.11	25.13 \pm 0.04	25.00 \pm 0.05	24.95 \pm 0.02	24.90 \pm 0.04	24.71 \pm 0.20	24.92 \pm 0.04	24.23 \pm 0.01	24.16 \pm 0.06	23.77 \pm 0.01	23.69 \pm 0.06	22.48 \pm 0.08	-99.99
22	25.11 \pm 0.15	24.12 \pm 0.02	23.85 \pm 0.02	23.77 \pm 0.01	23.69 \pm 0.02	23.55 \pm 0.09	23.31 \pm 0.01	22.76 \pm 0.00	22.72 \pm 0.03	22.40 \pm 0.01	22.13 \pm 0.02	21.46 \pm 0.05	-99.99
23	24.00 \pm 0.01	23.25 \pm 0.02	23.22 \pm 0.01	23.20 \pm 0.01	23.18 \pm 0.02	23.27 \pm 0.05	23.11 \pm 0.01	22.81 \pm 0.01	22.70 \pm 0.03	22.44 \pm 0.01	22.35 \pm 0.03	21.98 \pm 0.07	-99.99
24	25.10 \pm 0.07	24.44 \pm 0.02	24.24 \pm 0.03	24.15 \pm 0.01	24.06 \pm 0.03	23.78 \pm 0.10	23.46 \pm 0.01	22.64 \pm 0.01	22.63 \pm 0.03	22.14 \pm 0.00	21.69 \pm 0.02	21.25 \pm 0.04	-99.99
25	25.37 \pm 0.28	24.41 \pm 0.02	24.27 \pm 0.02	24.25 \pm 0.01	24.22 \pm 0.02	24.18 \pm 0.13	24.12 \pm 0.02	23.74 \pm 0.01	23.78 \pm 0.08	23.44 \pm 0.01	23.41 \pm 0.07	22.64 \pm 0.12	-99.99
26	25.09 \pm 0.06	24.48 \pm 0.02	24.47 \pm 0.03	24.47 \pm 0.01	24.48 \pm 0.03	24.20 \pm 0.13	24.19 \pm 0.02	23.66 \pm 0.01	23.69 \pm 0.04	23.65 \pm 0.01	23.38 \pm 0.05	22.91 \pm 0.12	-99.99
27	24.57 \pm 0.05	23.81 \pm 0.02	23.56 \pm 0.01	23.57 \pm 0.01	23.58 \pm 0.02	-99.99	23.75 \pm 0.04	23.37 \pm 0.04	23.37 \pm 0.04	23.37 \pm 0.04	22.90 \pm 0.04	22.41 \pm 0.01	-99.99
28	26.23 \pm 0.14	25.55 \pm 0.05	25.47 \pm 0.07	25.39 \pm 0.05	25.32 \pm 0.06	24.90 \pm 0.22	24.80 \pm 0.16	24.38 \pm 0.01	24.35 \pm 0.14	24.33 \pm 0.14	23.92 \pm 0.13	22.92 \pm 0.12	-99.99
29	25.56 \pm 0.10	24.96 \pm 0.04	24.86 \pm 0.04	24.77 \pm 0.03	24.67 \pm 0.03	24.38 \pm 0.16	24.38 \pm 0.16	24.38 \pm 0.16	24.38 \pm 0.16	24.38 \pm 0.16	24.38 \pm 0.16	24.38 \pm 0.16	-99.99
30	-99.99	26.68 \pm 0.15	26.30 \pm 0.14	26.29 \pm 0.10	26.27 \pm 0.14	-99.99	25.79 \pm 0.21	25.79 \pm 0.21	24.66 \pm 0.11	23.77 \pm 0.05	23.55 \pm 0.06	23.09 \pm 0.14	-99.99
31	25.26 \pm 0.07	24.53 \pm 0.02	24.45 \pm 0.03	24.35 \pm 0.02	24.26 \pm 0.02	24.03 \pm 0.11	24.21 \pm 0.05	23.77 \pm 0.01	23.77 \pm 0.01	23.77 \pm 0.01	23.48 \pm 0.06	22.69 \pm 0.10	-99.99
32	25.32 \pm 0.37	24.19 \pm 0.02	23.90 \pm 0.02	23.85 \pm 0.02	23.80 \pm 0.02	23.64 \pm 0.11	23.38 \pm 0.04	23.38 \pm 0.04	23.38 \pm 0.04	23.38 \pm 0.04	23.08 \pm 0.04	22.08 \pm 0.04	18.76 \pm 0.25
33	25.15 \pm 0.23	24.04 \pm 0.03	23.82 \pm 0.02	23.91 \pm 0.02	24.00 \pm 0.05	23.69 \pm 0.07	23.85 \pm 0.05	23.85 \pm 0.05	23.06 \pm 0.04	22.04 \pm 0.02	22.04 \pm 0.02	21.62 \pm 0.05	-99.99
34	25.34 \pm 0.08	24.44 \pm 0.02	24.18 \pm 0.02	24.19 \pm 0.02	24.19 \pm 0.02	24.06 \pm 0.12	24.01 \pm 0.05	23.42 \pm 0.05	23.24 \pm 0.03	22.76 \pm 0.03	22.76 \pm 0.03	21.88 \pm 0.04	-99.99
35	-99.99	26.45 \pm 0.18	26.15 \pm 0.18	25.91 \pm 0.10	25.68 \pm 0.11	25.18 \pm 0.39	25.03 \pm 0.14	23.42 \pm 0.05	23.42 \pm 0.05	22.82 \pm 0.04	22.82 \pm 0.04	22.23 \pm 0.07	19.34 \pm 0.31
36	-99.99	25.54 \pm 0.06	25.26 \pm 0.06	25.13 \pm 0.07	25.00 \pm 0.04	24.83 \pm 0.22	24.31 \pm 0.11	23.50 \pm 0.04	23.50 \pm 0.04	23.50 \pm 0.04	23.50 \pm 0.04	22.23 \pm 0.07	-99.99
37	-99.99	25.99	26.51 \pm 0.18	26.08 \pm 0.09	25.65 \pm 0.08	-99.99	25.34 \pm 0.14	24.25 \pm 0.08	24.25 \pm 0.08	24.25 \pm 0.08	23.07 \pm 0.04	22.50 \pm 0.08	-99.99
38	25.89 \pm 0.12	24.71 \pm 0.04	24.47 \pm 0.04	24.39 \pm 0.03	24.32 \pm 0.03	24.39 \pm 0.20	23.98 \pm 0.06	23.98 \pm 0.06	23.19 \pm 0.04	22.47 \pm 0.04	22.47 \pm 0.04	22.03 \pm 0.08	19.48 \pm 0.33
39	-99.99	25.11 \pm 0.06	24.84 \pm 0.05	24.70 \pm 0.03	24.56 \pm 0.06	-99.99	24.21 \pm 0.06	23.70 \pm 0.06	23.70 \pm 0.06	23.70 \pm 0.06	23.06 \pm 0.05	22.49 \pm 0.09	-99.99
40	25.44 \pm 0.12	24.70 \pm 0.04	24.48 \pm 0.04	24.43 \pm 0.03	24.38 \pm 0.03	24.15 \pm 0.17	24.15 \pm 0.07	23.40 \pm 0.05	23.40 \pm 0.05	23.40 \pm 0.05	22.74 \pm 0.04	21.87 \pm 0.07	-99.99
41	-99.99	24.92 \pm 0.03	24.70 \pm 0.04	24.66 \pm 0.02	24.62 \pm 0.03	24.37 \pm 0.15	24.27 \pm 0.06	23.72 \pm 0.04	23.72 \pm 0.04	23.72 \pm 0.04	23.04 \pm 0.04	22.03 \pm 0.06	-99.99
42	26.11 \pm 0.16	25.26 \pm 0.05	25.09 \pm 0.05	25.16 \pm 0.04	25.22 \pm 0.05	24.75 \pm 0.22	24.66 \pm 0.08	23.30 \pm 0.02	23.30 \pm 0.02	23.30 \pm 0.02	23.42 \pm 0.06	22.81 \pm 0.12	-99.99
43*	24.70 \pm 0.06	23.80 \pm 0.02	23.65 \pm 0.02	23.59 \pm 0.01	23.53 \pm 0.02	23.22 \pm 0.08	23.10 \pm 0.03	22.22 \pm 0.02	22.22 \pm 0.02	22.22 \pm 0.02	21.14 \pm 0.01	20.67 \pm 0.02	17.73 \pm 0.16
44	-99.99	25.99	26.51 \pm 0.18	26.08 \pm 0.09	25.65 \pm 0.08	-99.99	25.87 \pm 0.21	25.87 \pm 0.21	25.14 \pm 0.17	25.14 \pm 0.17	23.43 \pm 0.05	22.71 \pm 0.10	-99.99
45	-99.99	25.16 \pm 0.05	25.03 \pm 0.05	25.07 \pm 0.05	25.07 \pm 0.05	24.							

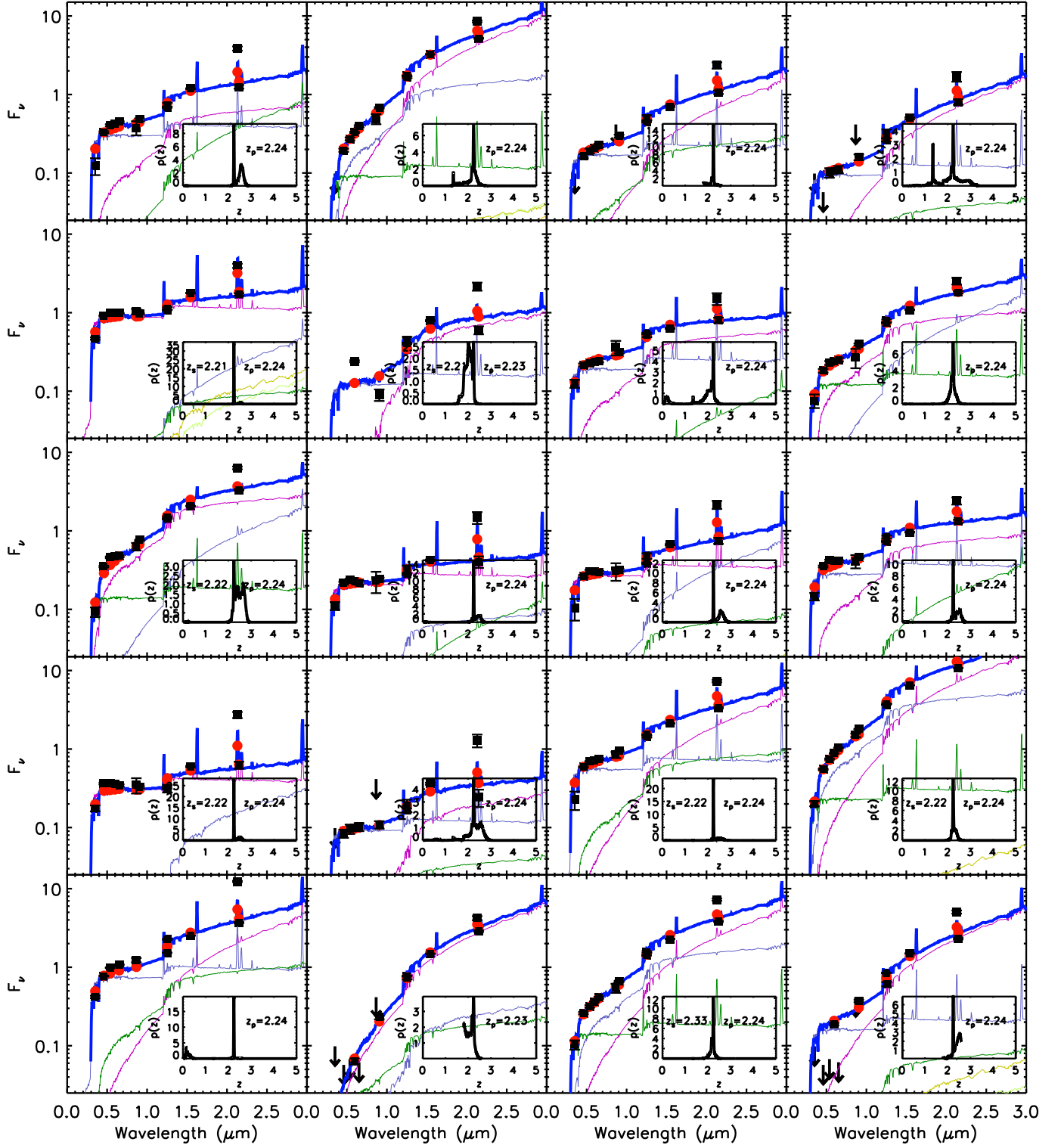


FIG. 3.— Best-fit SEDs of H α ELGs. The squares are the observed data points and circles are the best-fit data points from EAZY code (Brammer et al. 2008). The arrows show the upper limits of corresponding bands, which means the source is not detected or resolved in these bands. In each plan, the thick line shows the best-fit SED and light lines are the used templates; The inset plot shows the integrated probability of redshift.

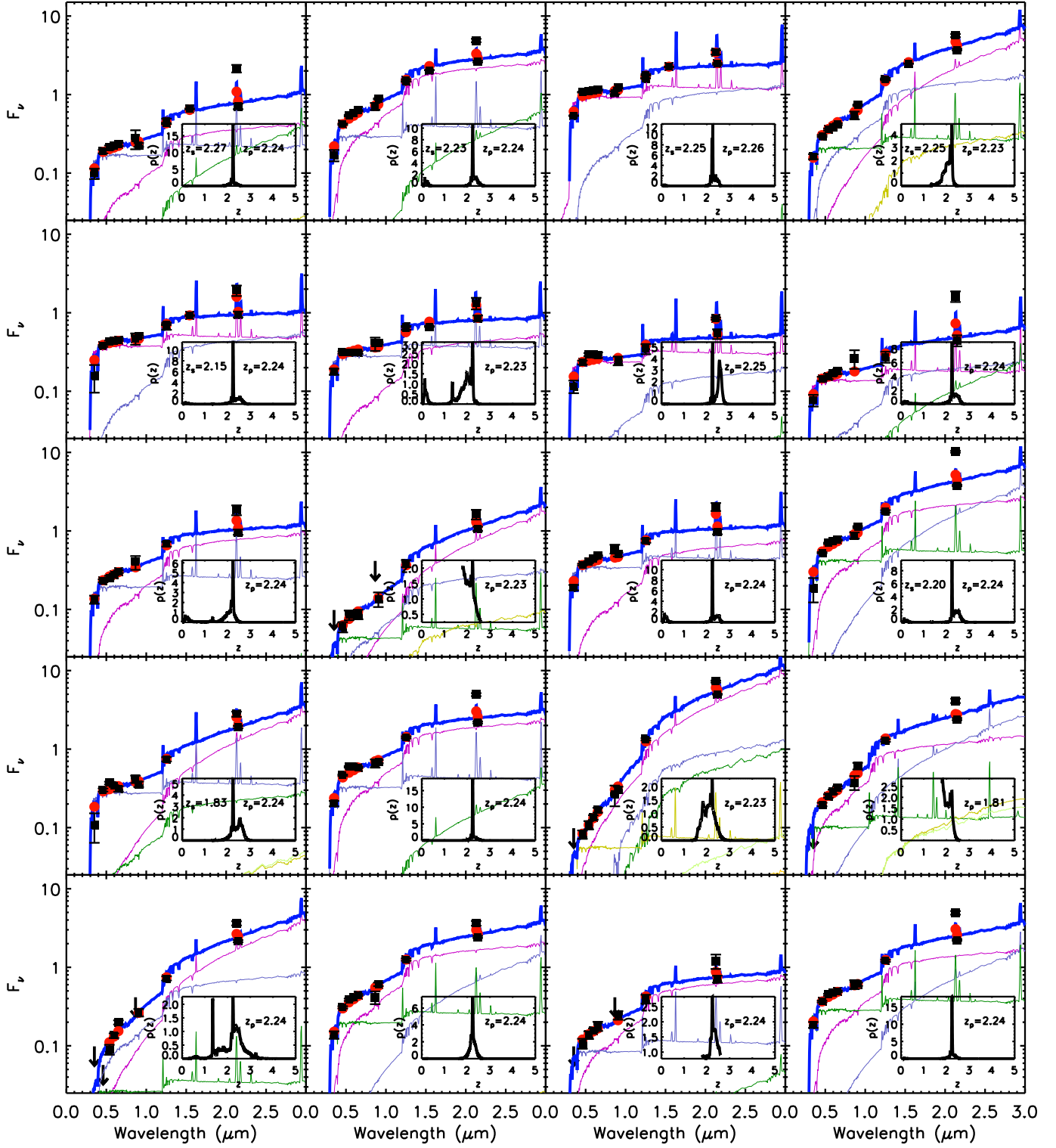


FIG. 3.— (Continued).

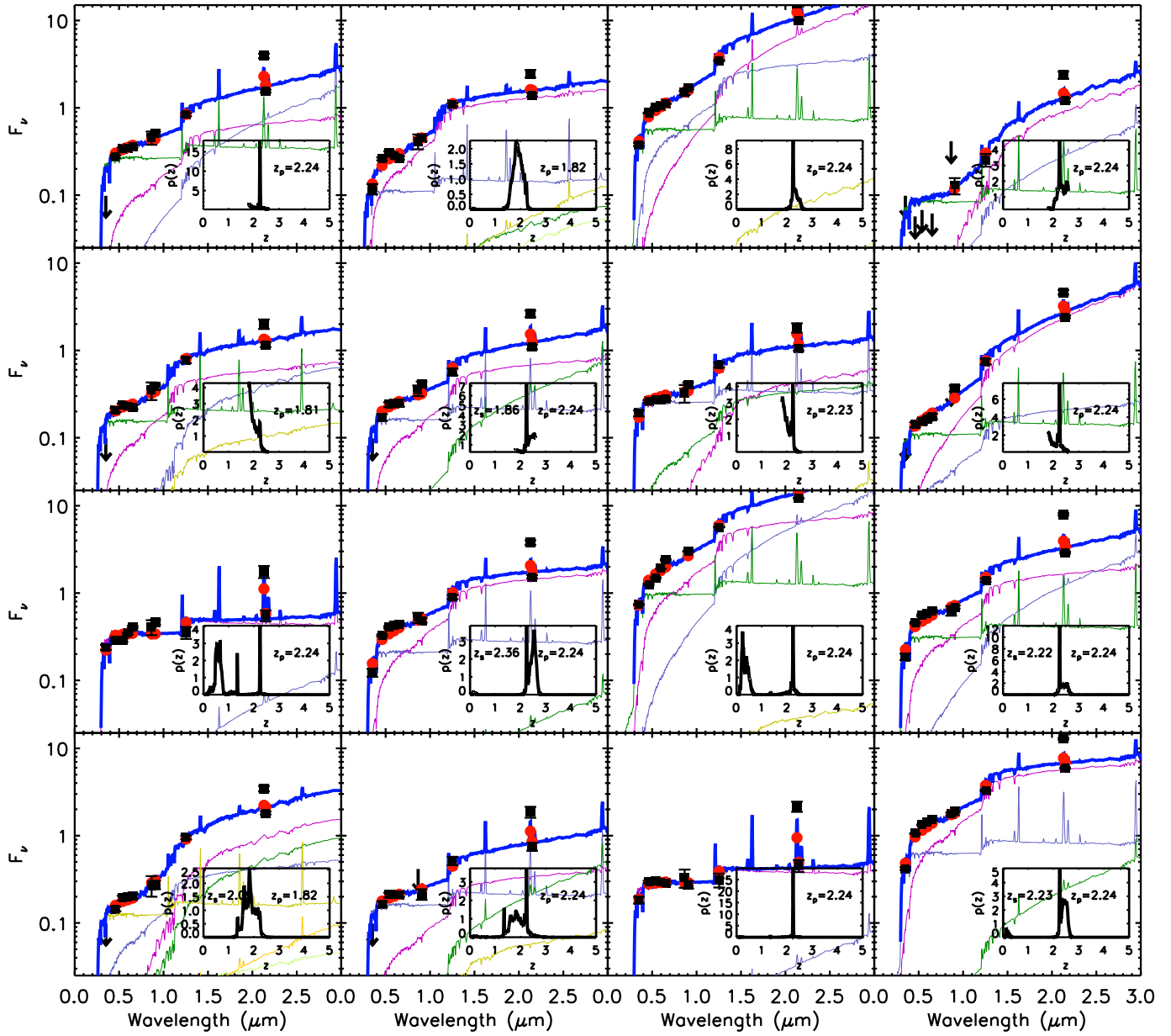


FIG. 3.— (Continued).

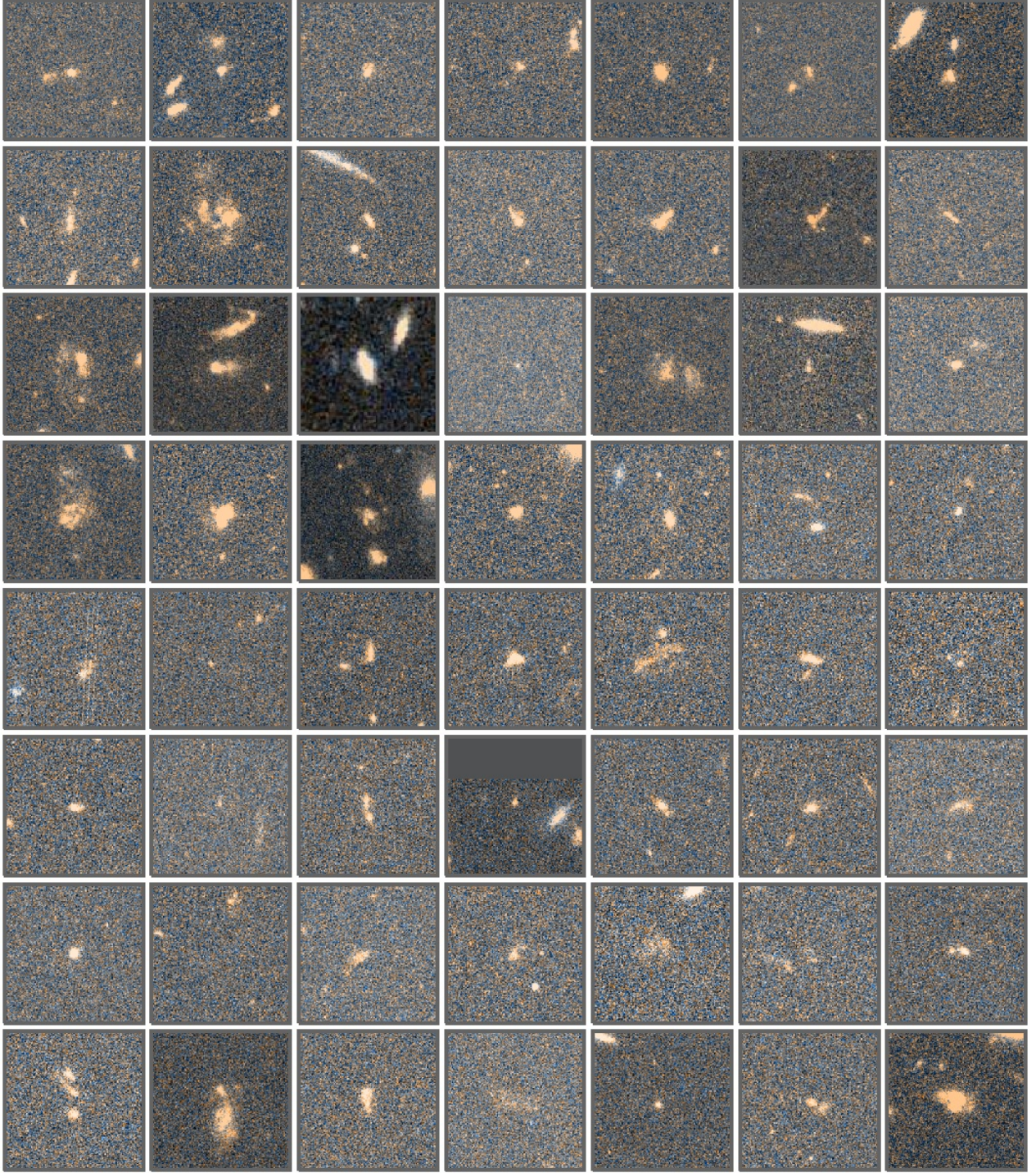


FIG. 4.— The $6'' \times 6''$ *HST* color images are made of ACS V_{606} and z_{850} from GEMS and GOODS. The 56 $H\alpha$ ELGs listed in Table 1 are given from left to right and top to bottom. One image (the 3rd from the top and 3rd from the left) is made of *HST*/WFC3 J_{125} and H_{160} from CANDELS due to no V_{606} observation.

We notice that roughly 10% (6/56) of $H\alpha$ ELGs exhibit an apparent offset ($> 0''.5$) between the central position in optical and NIR, indicating the complexity of morphologies in the rest-frame UV due to star formation activity and dust attenuation. Figure 5 shows *HST* $J_{125}+H_{160}$ color image stamps for the first 26 of the 56 $H\alpha$ ELGs. Still, our morphological classifications from V_{606}/z_{850} images are mostly consistent with those from J_{125}/H_{160} images for the 26 $H\alpha$ ELGs in GOODS-South. The similarity in morphology between the

rest-frame UV and the rest-frame optical for high- z SFGs are also claimed by other studies (e.g., Papovich et al. 2005; Law et al. 2012).

We also measure the morphological parameters Gini (the relative distribution of the galaxy pixel flux values) and M_{20} (the second-order moment of the brightest 20% of the galaxy's flux coefficients; Lotz et al. 2004) to quantify galaxy morphologies (Fang et al. 2012). Figure 6 shows the results. About half of our sample has $M_{20} > \sim -1.5$, satisfying the em-

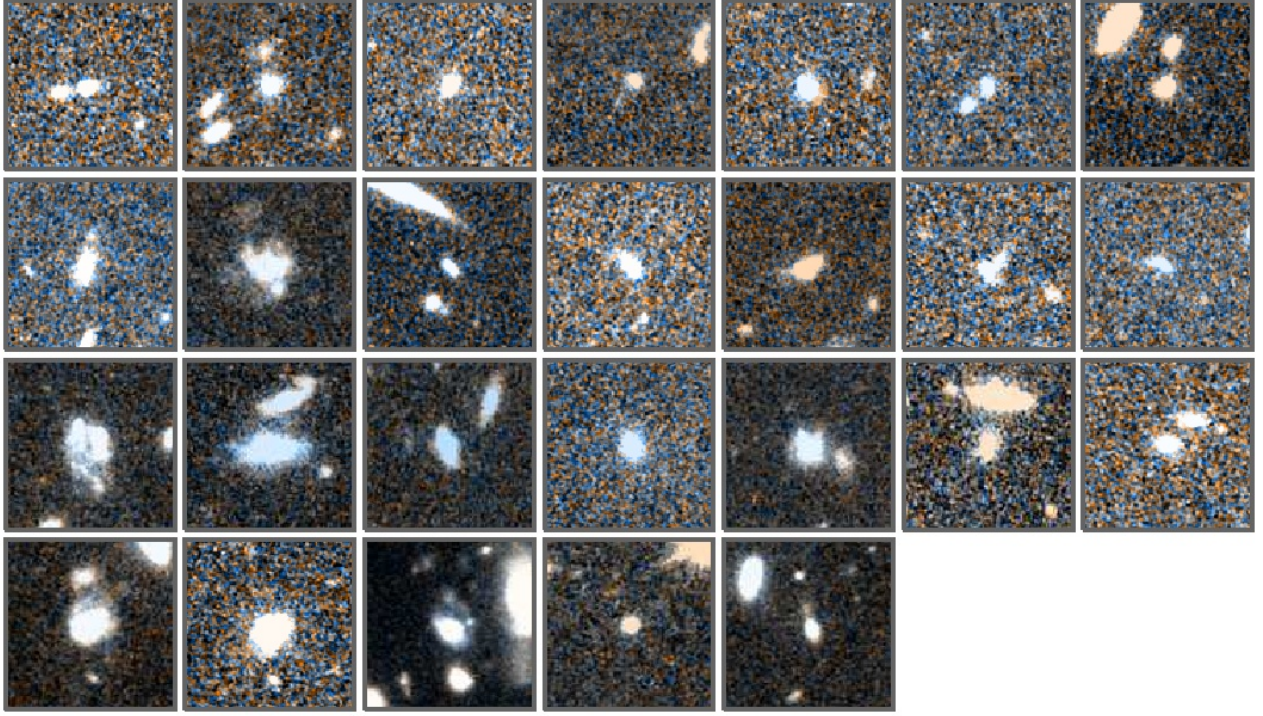


FIG. 5.— *HST*/WFC3 color images of the first 26 $H\alpha$ ELGs given in Table 1. The color images are made of J_{125} and H_{160} from CANDELS. Each thumbnail image has a size of $6'' \times 6''$ corresponding to $49 \text{ kpc} \times 49 \text{ kpc}$ at $z = 2.24$.

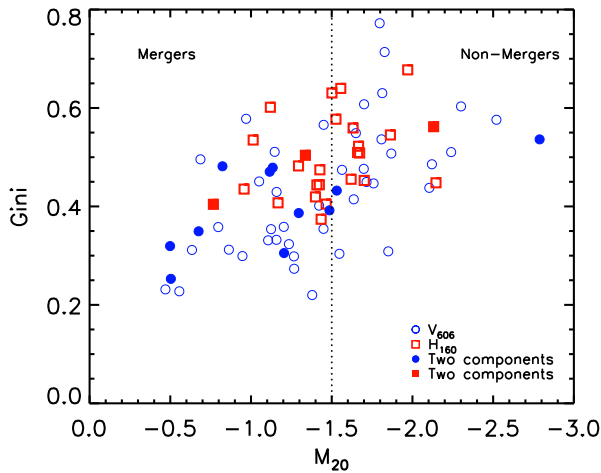


FIG. 6.— Gini vs. M_{20} coefficients for our sample of 56 $H\alpha$ ELGs. The circles represent the results derived from the *HST* F606W imaging data. The squares are the results from *HST* F160W imaging data for the 26 $H\alpha$ ELGs in GOODS-South. The solid circles and solid squares are the sample galaxies with two major components. The vertical line at $M_{20} \sim -1.5$ is the empirical delineation between mergers and non-mergers (Stott et al. 2013).

pirical cut for mergers (Stott et al. 2013). This is consistent with our result base on visual classification.

4.3. Dust Extinction

We estimate dust extinction from SEDs. Generally speaking, dust extinction mostly effects the young stellar population of a galaxy because new stars are formed in dusty environments. On the other hand, the young population can be divided into two components: unattenuated and attenuated. As described in Section 3.2, we made use of EAZY code to fit SEDs with models from combination of six represen-

tative galaxy templates. One in the six templates represents a young and dusty starburst with $A_V = 2.75$ mag. The other five templates represent distinct stellar populations without dust attenuation. Thus, the best-fit models to a galaxy SED implying not only the best photo- z , but also the percentage of each template in total (Brammer et al. 2008). Therefore, the young and dusty starburst template can be used to approximately trace the amount of dust attenuation in a galaxy. The total effective extinction A_V to the entire galaxy relies on the fraction of the dusty starburst component in the SED. Accordingly, we calculated A_V using the best-fit models composed of six templates given by EAZY. Figure 3 shows the decomposition of the best-fit models into the six components. Here the A_V is limited to $A_V \leq 2.75$ mag adopted by the dusty starburst template, although some $H\alpha$ -selected SFGs may be very dusty with $A(H\alpha)$ equal to several magnitudes (e.g., Garn et al. 2010; Sobral et al. 2012). We point out that this limitation is not crucial to our results and our main conclusions are not affected. We come back to this point in Section 5.

In addition, 12 of the 56 $H\alpha$ ELGs are found to have $24 \mu\text{m}$ counterparts. The $24 \mu\text{m}$ catalog is extracted from deep *Spitzer* $24 \mu\text{m}$ imaging of the Far-Infrared Deep Extragalactic Legacy survey (Dickinson & FIDEL Team 2007) using the PSF-fitting method of Zheng et al. (2006). The 3σ detection limit is $24.6 \mu\text{Jy}$, corresponding to the 50% completeness limit. The cross correlation between the two catalogs is done with a matching radius of $1''.2$. We list their $24 \mu\text{m}$ magnitudes in Table 1. We find that all the 12 objects have extinction > 1 mag and SFRs $> 20 M_\odot \text{ yr}^{-1}$ (see Section 4.4). The 12 sample targets are indeed dusty starburst galaxies. This confirms that our method works well in estimating dust extinction.

4.4. $H\alpha$ Luminosities and SFRs

TABLE 2
PHYSICAL PARAMETERS OF OUR SAMPLE OF H α ELGS

ID	Photo- z	Spec- z	A(H α) (mag)	log H α (erg s $^{-1}$)	log (M/M_{\odot})	Morphology ^a
1	2.25	...	1.07	42.99	9.95	1
2	2.24	...	1.92	43.39	10.75	2
3	2.24	...	1.70	42.94	9.42	4
4	2.24	...	2.00	42.87	9.54	5
5	2.25	2.21	0.65	42.76	9.33	2
6	2.24	2.22	0.00	42.22	9.81	1
7	2.24	...	0.36	42.25	9.81	1
8	2.24	...	1.40	42.52	10.15	2
9	2.25	2.23	1.06	43.17	10.62	3
10	2.25	...	0.67	42.52	9.21	4
11	2.25	...	1.41	42.86	9.61	2
12	2.25	...	0.64	42.46	9.91	2
13	2.25	2.22	0.00	42.46	9.35	2
14	2.24	...	0.00	42.19	9.14	3
15 ^b	2.24	2.23	1.67	43.55	10.69	2
16 ^b	2.24	2.22	1.73	44.00	11.36	2
17	2.24	...	1.58	43.47	10.35	3
18	2.24	...	2.10	42.99	10.53	5
19	2.24	2.34	1.70	43.30	10.74	3
20	2.24	...	2.10	43.31	10.57	3
21	2.24	2.28	0.95	42.70	9.76	4
22	2.24	2.23	0.53	42.70	10.23	3
23	2.26	2.26	0.03	42.28	10.14	2
24	2.24	2.25	1.62	43.14	10.93	3
25	2.25	2.15	0.04	42.17	9.50	4
26	2.23	...	0.04	41.91	9.36	4
27	2.26	...	0.16	42.17	9.98	1
28	2.25	...	0.93	42.55	9.45	4
29	2.24	...	0.05	42.12	9.87	3
30	2.24	...	1.83	42.53	9.82	5
31	2.25	...	0.01	42.13	9.39	1
32	2.25	2.21	1.32	43.43	10.49	2
33	2.24	1.83	1.81	43.11	10.53	1
34	2.24	...	0.36	42.63	10.21	1
35	2.24	...	1.93	43.14	10.91	5
36	1.82	...	1.33	42.77	9.94	4
37	2.24	...	1.87	42.86	10.17	5
38	2.24	...	1.05	42.58	10.38	3
39	2.25	...	0.18	42.19	9.89	5
40	2.24	...	1.14	42.75	10.22	2
41	2.24	...	1.40	43.01	9.86	4
42	1.83	...	0.18	42.08	9.51	2
43 ^b	2.25	...	1.77	43.50	11.14	4
44	2.25	...	1.06	42.52	10.23	5
45	1.82	...	0.00	42.06	9.86	3
46	2.24	1.87	1.08	42.77	9.77	3
47	2.24	...	0.09	42.03	9.83	3
48	2.24	...	2.09	43.18	10.58	3
49	2.24	...	0.54	42.41	8.40	1
50	2.25	2.36	0.12	42.57	10.02	1
51	2.24	...	1.44	43.10	10.71	1
52	2.25	2.22	1.32	43.28	10.52	2
53	1.83	2.10	0.14	42.24	9.91	5
54	2.24	...	1.05	42.50	9.46	4
55	2.24	...	0.42	42.45	9.26	1
56	2.25	2.23	0.23	43.02	10.64	2

^a 1: Two components; 2: merger; 3: spiral/diffuse/clumpy; 4: compact; 5: UV-faint. ^b Three X-ray sources (corresponded ID = 435, 29 and 399 in the *Chandra* catalog).

Following Ly et al. (2011), we derive H α + [N II] flux from the narrow-band excess $K_s - H_2S1$ and K_s total magnitude using the formula

$$F_L = \Delta\text{NB} \frac{f_{\text{NB}} - f_{K_s}}{1 - (\Delta\text{NB}/\Delta K_s)}, \quad (2)$$

where f_{NB} and f_{K_s} are fluxes given in the units of erg s $^{-1}$ cm $^{-2}$ Å $^{-1}$ for the H_2S1 - and K_s -band with filter width $\Delta\text{NB} = 293$ Å and $\Delta K_s = 3250$ Å, respectively.

We use [N II]/H α = 0.117 to correct the contribution of [N II] $\lambda\lambda 6548, 6583$ and obtain the observed H α fluxes (Hayes et al. 2010). The selection cut $\text{EW} > 50$ Å together with the 5σ depths of $H_2S1 = 22.8$ and $K_s = 24.8$ determines an H α

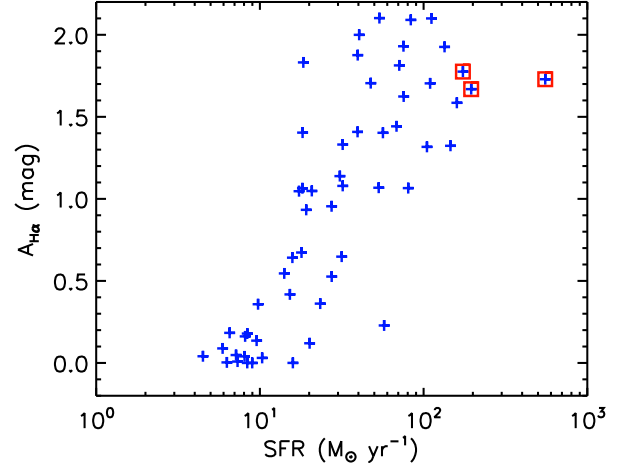


FIG. 7.— Relationship between SFR and SED-derived extinction for our sample of 56 H α ELGs at $z = 2.24$. The red squares mark three X-ray sources.

flux detection limit $> 2.1 \times 10^{-17}$ erg s $^{-1}$ cm $^{-1}$ Hz $^{-1}$. Differing from low- z SFGs, the high- z ones seem to show little difference between extinction derived from continuum and nebular lines (Erb et al. 2006b). We employ the Calzetti extinction law to estimate attenuation to H α line $A(\text{H}\alpha)$ from A_V which is derived from the SED modeling (Calzetti et al. 2000). The intrinsic H α fluxes are estimated from the observed H α fluxes with correction for extinction $A(\text{H}\alpha)$. Then H α luminosity is calculated with $z = 2.24$.

The H α luminosity is an estimator of SFR. We follow Kennicutt & Evans (2012, hereafter K12) to calculate SFR using

$$\log(\text{SFR}/M_{\odot} \text{ yr}^{-1}) = \log L_{\text{H}\alpha} - 41.27, \quad (3)$$

where $L_{\text{H}\alpha}$ is the extinction-corrected H α luminosity in the units of erg s $^{-1}$. The SFR is calibrated with STARBURST99 model (Leitherer et al. 1999) and Kroupa IMF, differing from that given in Kennicutt (1998, hereafter K98). Table 2 in Kennicutt & Evans (2012) gives the conversion between K12 and K98 calibrations. For H α , $\text{SFR}_{\text{K12}}/\text{SFR}_{\text{K98}} = 0.68$.

Figure 7 shows the estimated SFR versus H α extinction. The data points spread mainly from 3 to 300 $M_{\odot} \text{ yr}^{-1}$ in SFR and from 0 to 2.2 mag in H α extinction $A(\text{H}\alpha)$. A correlation between SFR and H α extinction is apparent. The increase of extinction at an increasing SFR found for H α ELGs is also seen for low- z SFGs (e.g., Garn & Best 2010) and high- z SFGs (Ly et al. 2012; Sobral et al. 2012; Domínguez et al. 2013; Kashino et al. 2013).

4.5. Stellar Masses

The software FAST (Fitting and Assessment of Synthetic Templates; Kriek et al. 2009) is used to estimate stellar mass for our sample. The stellar population synthesis (SPS) models from Maraston (2005) and a Kroupa IMF (Kroupa 2001) are adopted. We fit the SPS models with exponentially declining star formation histories and the star formation timescale τ from 10 Myr to 10 Gyr in steps of 0.5 dex. The metallicity is fixed to solar ($Z = 0.02$) and the dust extinction is modeled by the Calzetti reddening law, with A_V from 0 to 3 mag in steps of 0.01 mag. The ages of the model stellar populations range from 0.1 Myr to the age of the universe. The best photo- z from EAZY is taken as input to FAST (see Kriek et al. 2009 for more details). Figure 8 shows the distribution of our sample galaxies in stellar mass and SFR. Three X-ray sources

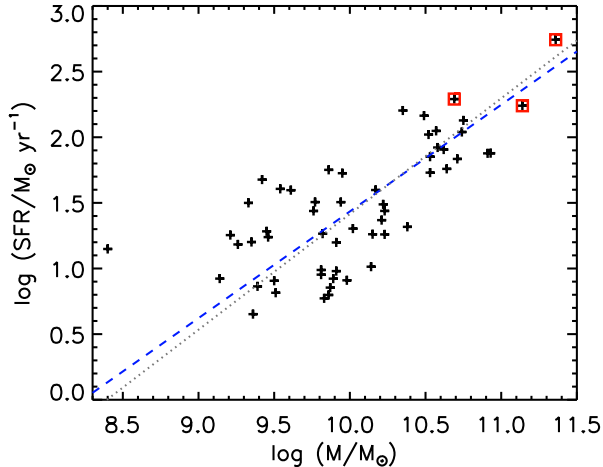


FIG. 8.— The Mass-SFR relation of our 56 $H\alpha$ ELGs. The three red squares are X-ray-detected AGNs. The blue dashed line is a linear fit to the mass-SFR relation, giving a best-fit slope of 0.81. The gray dotted line is the fit without the lowest stellar mass one, giving a best-fit slope of 0.88. The three X-ray sources are removed in both fittings.

are marked with red squares. The vast majority of the sample galaxies have a stellar mass $9 < \log(M/M_\odot) < 11$. The object has the lowest stellar mass $\log(M/M_\odot) = 8.40$ is faint in the K_s -band but with a high EW and very blue color. From Figure 8, we can see that the $H\alpha$ ELGs exhibit a correlation between stellar mass and SFR, which is known as the main sequence of SFGs (e.g., Elbaz et al. 2007; Daddi et al. 2007; Wuyts et al. 2011b). The dashed line describes the best fit to the mass-SFR correlation (three X-ray sources are removed), having a slope of 0.81. The scatter of this relation is 0.35 dex.

5. THE $H\alpha$ LF AT $Z = 2.24$

One of our goals is to revisit the $H\alpha$ LF and examine the influence of extinction correction. First, we commit Monte Carlo simulation to quantify the incompleteness of sample selection. After that, we determine the function of intrinsic $H\alpha$ luminosities at $z = 2.24$ using our sample of 53 X-ray-undetected $H\alpha$ galaxies. Finally, we show that a constant extinction correction to the observed $H\alpha$ luminosities results in an $H\alpha$ LF similar to the results in previous works.

5.1. Completeness

A Monte Carlo simulation is used to derive the detection completeness as a function of intrinsic $H\alpha$ luminosity. We assume that the intrinsic $H\alpha$ LF is described by a Schechter function with $L_{H\alpha}^* = 10^{42.88}$, $\alpha = -1.60$ and $\log\phi^* = -1.79$ from Sobral et al. (2013). The H_2S1 filter centered at $\lambda_c = 2.130 \mu\text{m}$ has a width of $\Delta\lambda = 0.0293 \mu\text{m}$, corresponding to $2.225 < z < 2.267$ for $H\alpha$. We use the averaged volume, corresponding to this redshift bin, as our effective volume. The brighter ELGs are detectable over a wider range of the filter transmission than the faint one. Therefore, we adopt a wider redshift span of $2.2 < z < 2.29$ to account for the entire wavelength coverage of the filter curve in our simulation. Then we can estimate the contamination rate of bright ELGs from low- z ($2.200 < z < 2.225$) and high- z ($2.267 < z < 2.290$). We generated a mock catalog of 30 million galaxies with $H\alpha$ emission lines satisfying the given LF and the given redshift range. In practice, the simulated galaxies are divided into 30 redshift bins. In each redshift bin, the galaxies are divided again into 500 bins between $40 < \log(L_{H\alpha}/\text{erg s}^{-1}) < 50$.

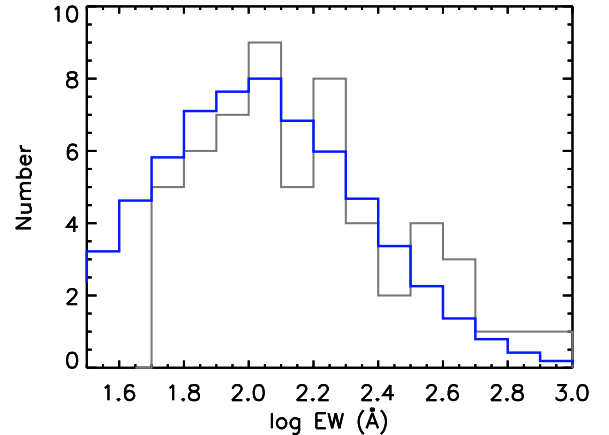


FIG. 9.— Comparison of the modeled and observed EW distributions. The blue thick line shows the best matched model with mean $\log(\text{EW}_{\text{rest}}) = 2.00$ and $\sigma[\log(\text{EW}_{\text{rest}}/\text{\AA})] = 0.35$ and is scaled to match the observed distribution (gray line).

Each bin contains on average 2000 galaxies. The contribution of $[\text{N II}]$ is added to the simulated $H\alpha$ using $[\text{N II}]/H\alpha = 0.117$. Dust attenuation is applied following the relation given in Figure 7 with a scatter of 0.38 in $A(H\alpha)$ taken into account. Furthermore, a Gaussian line profile with $\sigma = 200 \text{ km s}^{-1}$ is adopted to convolve $H\alpha$ at given redshifts with the H_2S1 filter transmission curve to simulate the observed $H\alpha + [\text{N II}]$ fluxes.

To link $H\alpha + [\text{N II}]$ of a given flux to H_2S1 and K_s magnitudes of a galaxy, one needs to know the EW of the line. The intrinsic distribution of EW of $H\alpha + [\text{N II}]$ is fairly similar to the observed distribution of rest-frame EW (Lee et al. 2007). We assume a log-normal distribution of EW for $H\alpha + [\text{N II}]$ following Ly et al. (2011). Since the observed EWs of our sample are affected by noise as shown in Figure 1, we take the noise effects into account and infer the best-matched distribution as follows. A set of log-normal EW distributions are generated with the mean $\log(\text{EW}_{\text{rest}})$ spanning between 1.8 and 2.3 and the spread $\sigma[\log(\text{EW}_{\text{rest}}/\text{\AA})]$ between 0.15 and 0.65. A step of 0.1 dex is adopted for the two parameters. Assuming that the flux of $H\alpha + [\text{N II}]$ is not correlated with its EW, we randomly assign EWs satisfying a modeled EW distribution to the observed $H\alpha + [\text{N II}]$ fluxes and give H_2S1 and K_s magnitudes. Added to the photon noise and sky background noise from our H_2S1 and K_s images (see also Ly et al. 2012), the simulated galaxies can be selected by $H_2S1 - K_s$ selection criteria as shown in Figure 1. By doing so, we model the ‘observed’ EW distribution for each of input intrinsic EW distributions under the same conditions as our H_2S1 and K_s observations. Comparing the modeled EW distributions with the observed EW distribution of our sample and minimizing the χ^2 , we obtain the intrinsic EW distribution best matching the observed EW distribution. The model with mean $\log(\text{EW}_{\text{rest}}) = 2.00$ and $\sigma[\log(\text{EW}_{\text{rest}}/\text{\AA})] = 0.35$ best reproduces the observed distribution of our sample galaxies. We show the best-matched mode in comparison with the observed distribution in Figure 9. This distribution is taken to randomly assign EWs to the mock catalog of simulated $H\alpha + [\text{N II}]$ galaxies, thus making it possible to obtain H_2S1 and K_s magnitudes.

Accounting for the photon noise and sky noises from our H_2S1 and K_s images, the simulated $H\alpha$ ELGs are selected us-

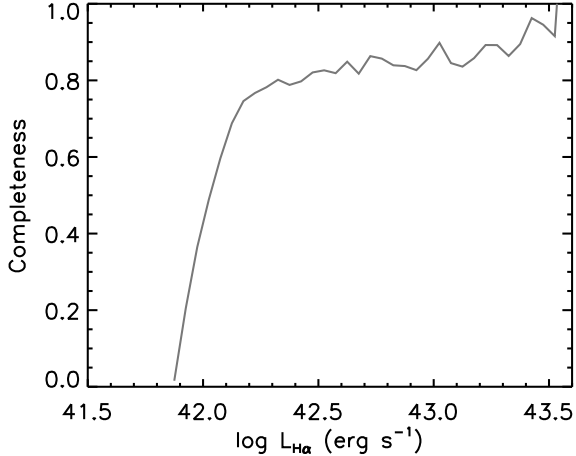


FIG. 10.— Completeness as a function of H α luminosity.

ing the criteria as shown in Figure 1. By doing so, we obtained the fraction of the mock galaxies picked up by our selection at given intrinsic H α fluxes, giving the completeness as a function of the intrinsic H α luminosity shown in Figure 10. Because the completeness curve is insensitive to the input Schechter function in the simulation, we employ the completeness curve given in Figure 10 to determine H α LF using our sample. Note that the volume correction and completeness estimate for our sample root on the redshift bin $2.225 < z < 2.267$ and the final completeness curve accounts for all major effects involved in our observation and selection.

5.2. Determination of H α LF

We determine the H α LF at $z = 2.24$ using our sample of 53 H α ELGs. Three X-ray sources are excluded to avoid AGN contamination. A volume of $5.40 \times 10^4 \text{ Mpc}^3$ is calculated from the coverage of 383 arcmin^2 of our sample and a redshift span $2.225 < z < 2.267$. By dividing our sample into five bins in $\log(L_{\text{H}\alpha})$ from 42.0 to 43.5 and taking the completeness correction, we obtained our H α LF data points as shown in Figure 11. The error bars represent mainly the Poisson noise. We fit the data points with a Schechter function (Schechter 1976) in the form of

$$\Phi(\log L)d(\log L) = \ln(10) \Phi^* 10^{(\alpha+1)(\log L - \log L^*)} \exp[-10^{\log L - \log L^*}] d(\log L), \quad (4)$$

where L^* is the characteristic luminosity, Φ^* is the normalization, and α is the faint-end power-law index. The standard χ^2 minimizer is used in the fitting and the errors are the formal 1σ statistical errors on the parameters. Since all our data points place in the power-law region of the LF, only the faint-end slope can be reliably constrained. The best-fit faint-end slope is $\alpha = -1.36 \pm 0.32$.

It is worth noting that H α LF traces SFR function. With the main sequence of SFGs, i.e., the tight correlation between SFR and stellar mass, one would expect that the H α LF is also connected with SMF. We use the mass-SFR relation of SFGs at $z \sim 2$ (slope = 1 and $\log(\text{SFR}/M_\odot \text{ yr}^{-1}) = 2.45$ at $\log(M/M_\odot) = 11.0$) from Wuyts et al. (2011b) to convert an SMF to an SFR function, and use Equation 3 to translate the SFR function into an H α LF. Three SMFs of SFGs are adopted for comparison: $1.5 < z < 2.0$ from Ilbert et al. (2010), $2.0 < z < 2.5$ from Karim et al. (2011) and $1.8 <$

$z < 2.2$ from Brammer et al. (2011). The H α LFs converted from the SMFs are plotted in Figure 11. Apparently, these H α LFs are in very good agreement with our H α LF in shape, although they tend to be slightly higher. The stellar mass at the “knee” of the SMF is $M^* = 10^{10.95 \pm 0.03} M_\odot$ in Karim et al. (2011), corresponding $L^* = 10^{43.67} \text{ erg s}^{-1}$ for H α LF. Taking this value, we refit H α LF with the Schechter function and also with three X-ray sources removed, giving the best-fit result $\log \Phi^* = -3.27^{+0.14}_{-0.22}$ and $\alpha = -1.31 \pm 0.16$. In summary, all of our two fittings of H α LF give a consistent faint-end slope. Therefore, we conclude that the faint-end slope with the value of $\alpha = -1.3$ for H α LF is robust, despite our sample not being large, and provides poor constraint on the bright-end of H α LF. Therefore, the limitation of $A_V \leq 2.75 \text{ mag}$ in estimating dust extinction as we described in Section 4.3 does not affect our main conclusions.

The H α LFs at $z = 2.23$ from previous works are also shown in Figure 11 for comparison. Note that a constant extinction correction was adopted in these studies ($A(\text{H}\alpha) = 1 \text{ mag}$; Geach et al. 2008, Hayes et al. 2010, Sobral et al. 2013; $A(\text{H}\alpha) = 0.5 \text{ mag}$; Lee et al. 2012). Large discrepancies can be seen between our H α LF and others: ours is much shallower at the faint end and higher at the bright end. We argue that the discrepancies are mostly attributed to the difference in extinction correction. A fixed correction does not change the shape of an observed H α LF. Our correction for extinction on an individual basis is able to recover heavily attenuated SFGs with intrinsically luminous H α from the faint end of the H α LF. This enables the data points to spread into a wider luminosity range, resulting a decrease at the faint end and an increase at the bright end.

We rebuild an H α LF based on our sample but with a constant extinction correction ($A(\text{H}\alpha) = 1 \text{ mag}$). Simulation is carried out with the constant extinction to derive the completeness as a function of H α luminosity. We present the rebuilt H α LF in Figure 12. We also fit it with a Schechter function, giving a best-fit faint-end slope $\alpha = -1.59 \pm 0.26$. This is consistent with the typical value of $\alpha \sim -1.6$ given in other works. The same as in Figure 11, the H α LFs from previous studies are shown for comparison. A good agreement between these H α LFs is seen within uncertainties. It becomes clear that extinction correction is key in determining the H α LF. Furthermore, the extinction correction must be done on an individual basis.

6. DISCUSSION AND CONCLUSION

We have described a search for H α ELGs using deep H_2S1 imaging combined with deep K_s imaging data of ECDIFS. In total 140 emission-line candidates are identified. The deep optical and NIR imaging data in the ECDIFS are utilized to construct broad-band SEDs and derive photo- z , stellar mass and extinction. We identify 56 H α emitters with H α flux $> 2.1 \times 10^{-17} \text{ erg s}^{-1} \text{ cm}^{-1} \text{ Hz}^{-1}$. Three of the 56 are X-ray sources detected in the *Chandra* 4 Ms observation and two of them host an AGN in terms of their X-ray luminosities. The stacked X-ray luminosity of the rest is consistent with that of SFGs. In our sample, only $\sim 4\%$ are contaminated by AGN, although obscured AGNs individually undetected in the current X-ray observation may still present in some of the sample galaxies. However, the obscured AGNs are unlikely to be responsible for exciting H α line. As a result, our sample is clean for studying the properties of H α ELGs and determining the H α LF.

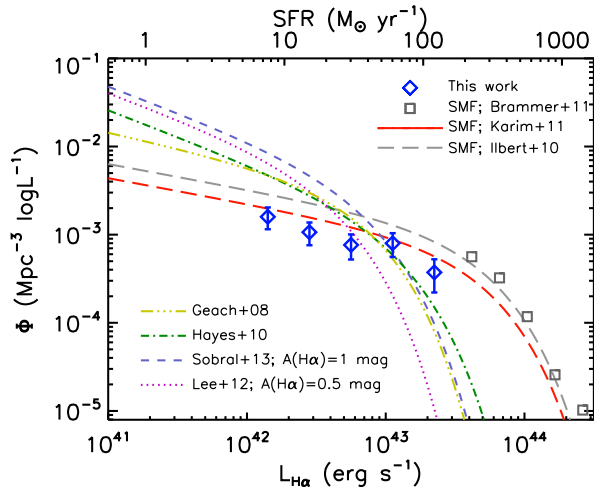


FIG. 11.— $H\alpha$ LF at $z = 2.24$. The blue diamonds are data points based on individual extinction correction derived from SED modeling. The error bars are determined by Poisson noise. The dashed lines are the SMF of SFGs at $1.5 < z < 2.0$ from Ilbert et al. (2010) and that at $2.0 < z < 2.5$ from Karim et al. (2011). The gray squares are the SMF of SFGs at $1.8 < z < 2.2$ from Brammer et al. (2011). The thin lines show representative $H\alpha$ LFs at $z = 2.23$ in the literature.

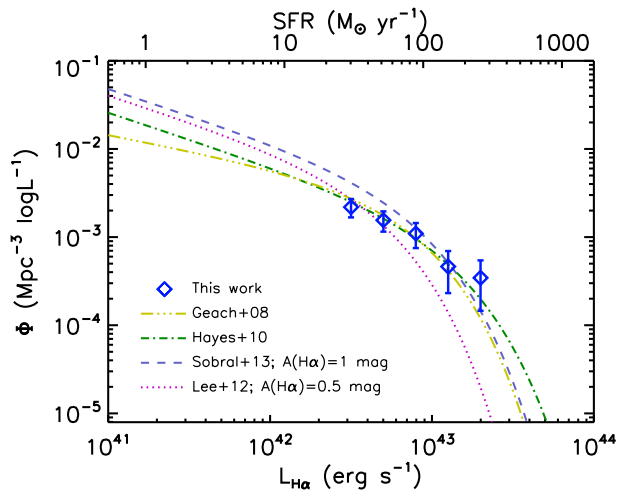


FIG. 12.— $H\alpha$ LF derived with constant extinction correction. The blue diamonds are the data points from this work. The thin lines show the $H\alpha$ LFs from previous works with constant extinction correction: $A(H\alpha) = 0.5$ mag in Lee et al. (2012) and $A(H\alpha) = 1$ mag in other works.

HST/ACS imaging reveals that nearly half of our $H\alpha$ ELGs are either mergers or close pairs. A similar merger fraction was suggested by Conselice et al. (2003) for SFGs at $z \sim 2$, although large uncertainties exist in measuring merger fraction as a function of redshift (e.g., $\sim 30\%$ for $H\alpha$ ELGs at $z = 2.23$ by Stott et al. 2013). A significant fraction (14%) of the $H\alpha$ ELGs are too faint to be resolved in the rest-frame UV. These UV-faint ones are confirmed to be heavily-obscured SFGs by SED modeling. The remaining one third exhibit extended or compact morphologies. We note that the morphological properties of our $H\alpha$ ELGs are consistent with those of high- z SFGs (e.g., Lotz et al. 2006; Ravindranath et al. 2006; Conselice et al. 2011). Our results reveal that merging/interacting processes play a key role in regulating star formation in typical SFGs at cosmic epoch $z \sim 2-3$.

Our sample of 56 $H\alpha$ ELGs are representative of SFGs at $z \sim 2-3$ in many aspects. SFGs are found to be more ob-

scured at higher SFR (e.g., Bothwell et al. 2011, for $z \sim 0$; Zheng et al. 2007; Ly et al. 2012; Domínguez et al. 2013 for high- z). We also find such a tendency among $H\alpha$ ELGs as shown in Figure 7. Our extinction is estimated from SEDs. It is important to note that the SED-derived extinction tends to be lower than the true case represented by the IR to UV luminosity ratio $L_{\text{IR}}/L_{\text{UV}}$, especially at the high-SFR end (Wuyts et al. 2011a). This is understandable because in starbursts, parts of newly formed stars are deeply buried in dusty molecular clouds and can only be traced by the IR emission (e.g., Swinbank et al. 2004; Sedgwick et al. 2013). Adding this correction would enhance the correlation between extinction and SFR. The mass-SFR relation is well-established from the present day all the way to $z \sim 3$ (e.g., Elbaz et al. 2007; Daddi et al. 2007). The slope of the mass-SFR relation at $z \sim 2$ is close to unity (Wuyts et al. 2011b). As shown in Figure 8, $H\alpha$ ELGs follow the mass-SFR relation of SFGs, giving a slope of 0.81. We argue that the shallower slope of the $H\alpha$ ELGs is likely attributed to the underestimate of extinction at high end.

The correction for extinction on an individual basis is vital to determining the shape of the $H\alpha$ LF. With extinction correction for individual sample galaxies, we build the $H\alpha$ LF at $z = 2.24$. The completeness as a function of $H\alpha$ luminosity is carefully estimated via Monte Carlo simulation and is applied to the observed LF. Our sample is not large and unable to give a good constraint on the bright-end of $H\alpha$ LF. A shallow faint-end slope of $\alpha = -1.32 \pm 0.24$ is robustly obtained, compared to the typical value of ~ -1.6 given by previous studies in which correction for a constant extinction is often adopted (Geach et al. 2008; Hayes et al. 2010; Sobral et al. 2013). We have shown that a steep faint-end slope is inevitable when a fixed extinction is applied. Garn et al. (2010) computed the $H\alpha$ LFs at $z = 0.84$ with correction for SFR-dependent extinction and constant ($A(H\alpha) = 1$ mag) extinction, respectively, finding that the former gives a shallower faint-end slope. It is obvious that the constant extinction correction is not a good approximation because it will overestimate the extinction in faint $H\alpha$ ELGs and severely underestimate the extinction for brightest ones. Resolving heavily-attenuated SFGs from the emitters with faint $H\alpha$ naturally leads to a decline at the faint end of an $H\alpha$ LF. The extinction is broadly correlated with SFR, stellar mass, and $H\alpha$ equivalent width (see also Garn et al. 2010; Garn & Best 2010; Ly et al. 2012; Domínguez et al. 2013; Kashino et al. 2013). To address which parameter is more fundamental in governing extinction is beyond the scope of this work.

We argue that $H\alpha$ LF at $z = 2.24$ mirrors the SMFs of SFGs at $z \sim 2$. We know that the SED-derived extinction tends to be underestimated. Therefore, our $H\alpha$ LF is likely underestimated too. Taking this into account, the agreement between our $H\alpha$ LF and these converted from SMFs is notably good. The evolution of SMFs or cosmic variance may also induce additional uncertainties. We emphasize that this finding is indeed a reflection of the main sequence of SFGs. The excellent agreement between the $H\alpha$ LF and the SMFs confirms that the main sequence has a slope close to unity. As a consequence, the $H\alpha$ -selection and the color-selection target on the same population of SFGs and naturally link the two branches of studies together.

On the other hand, the faint-end slope of $H\alpha$ LF signifies the relative contribution between galaxies with weak and luminous $H\alpha$, a measurement that is important to the understanding of star formation behavior over cosmic time

(e.g., Dutton et al. 2010). The faint-end of an LF is shaped by processes related to star formation, e.g., feedback from supernovae (Dekel & Silk 1986), radiatively driven winds (Springel & Hernquist 2003), and photons ionizing neutral gas (Kravtsov et al. 2004). The dependence of the faint-end slope of H α LF on extinction correction hints that UV LFs at high- z might be in a similar situation. For instance, Reddy & Steidel (2009) presented the UV LF at $z \sim 2-3$ with a faint-end slope of -1.73 . Since UV light is closely coupled with H α emission, we suspect that the faint-end of the UV LF would become shallower if careful extinction correction is taken into account.

We are grateful to the referee for his/her valuable comments and suggestions, which have improved our manuscript.

F.X.A acknowledges Cong Ma for his kind assistance. This research uses data obtained through the Telescope Access Program (TAP), which is funded by the National Astronomical Observatories and the Special Fund for Astronomy from the Ministry of Finance. This work is supported by the Strategic Priority Research Program "The Emergence of Cosmological Structures" of the Chinese Academy of Sciences (Grant No. XDB09000000) and National Basic Research Program of China (973 Program 2013CB834900). W-H.W. acknowledges the grant of National Science Council of Taiwan (102-2119-M-001-007-MY3). X.K. is supported by the National Natural Science Foundation of China (NSFC, Nos. 11225315 and 11320101002) and the Specialized Research Fund for the Doctoral Program of Higher Education (SRFDP, No. 20123402110037).

REFERENCES

- An, F. X., Zheng, X. Z., Meng, Y. Z., et al. 2013, *Sci China-Phys Mech Astron*, 56, 2226
- Atek, H., Malkan, M., McCarthy, P., et al. 2010, *ApJ*, 723, 104
- Bertin, E., & Arnouts, S. 1996, *A&AS*, 117, 393
- Bothwell, M. S., Kenicutt, R. C., Johnson, B. D., et al. 2011, *MNRAS*, 415, 1815
- Brammer, G. B., van Dokkum, P. G., & Coppi, P. 2008, *ApJ*, 686, 1503
- Brammer, G. B., Whitaker, K. E., van Dokkum, P. G., et al. 2011, *ApJ*, 739, 24
- Brinchmann, J., Charlot, S., White, S. D. M., et al. 2004, *MNRAS*, 351, 1151
- Bunker, A. J., Warren, S. J., Hewett, P. C., & Clements, D. L. 1995, *MNRAS*, 273, 513
- Caldwell, J. A. R., McIntosh, D. H., Rix, H.-W., et al. 2008, *ApJS*, 174, 136
- Calzetti, D., Armus, L., Bohlin, R. C., et al. 2000, *ApJ*, 533, 682
- Cardamone, C. N., van Dokkum, P. G., Urry, C. M., et al. 2010, *ApJS*, 189, 270
- Chapman, S. C., Blain, A. W., Smail, I., & Ivison, R. J. 2005, *ApJ*, 622, 772
- Colbert, J. W., Teplitz, H., Atek, H., et al. 2013, *ApJ*, 779, 34
- Conselice, C. J., Bershad, M. A., Dickinson, M., & Papovich, C. 2003, *AJ*, 126, 1183
- Conselice, C. J., Bluck, A. F. L., Ravindranath, S., et al. 2011, *MNRAS*, 417, 2770
- Daddi, E., Cimatti, A., Renzini, A., et al. 2004, *ApJ*, 617, 746
- Daddi, E., Dickinson, M., Morrison, G., et al. 2007, *ApJ*, 670, 156
- Dekel, A., & Silk, J. 1986, *ApJ*, 303, 39
- Dickinson, M., & FIDEL Team 2007, *BAAS*, 39, 822
- Domínguez, A., Siana, B., Henry, A. L., et al. 2013, *ApJ*, 763, 145
- Dutton, A. A., van den Bosch, F. C., & Dekel, A. 2010, *MNRAS*, 405, 1690
- Elbaz, D., Daddi, E., Le Borgne, D., et al. 2007, *A&A*, 468, 33
- Erb, D. K., Steidel, C. C., Shapley, A. E., et al. 2006, *ApJ*, 646, 107
- Fang, G., Kong, X., Chen, Y., & Lin, X. 2012, *ApJ*, 751, 109
- Fioc, M., & Rocca-Volmerange, B. 1997, *A&A*, 326, 950
- Franx, M., Labbé, I., Rudnick, G., et al. 2003, *ApJL*, 587, L79
- Garn, T., & Best, P. N. 2010, *MNRAS*, 409, 421
- Garn, T., Sobral, D., Best, P. N., et al. 2010, *MNRAS*, 402, 2017
- Gawiser, E., van Dokkum, P. G., Herrera, D., et al. 2006, *ApJS*, 162, 1
- Geach, J. E., Smail, I., Best, P. N., et al. 2008, *MNRAS*, 388, 1473
- Geach, J. E., Sobral, D., Hickox, R. C., et al. 2012, *MNRAS*, 426, 679
- Grogin, N. A., Kocevski, D. D., Faber, S. M., et al. 2011, *ApJS*, 197, 35
- Guo, K., Zheng, X. Z., & Fu, H. 2013, *ApJ*, 778, 23
- Hatch, N. A., Kurk, J. D., Pentericci, L., et al. 2011, *MNRAS*, 415, 2993
- Hayes, M., Schaerer, D., Östlin, G. 2010, *A&A*, 509, L5
- Hopkins, A. M., & Beacom, J. F. 2006, *ApJ*, 651, 142
- Hsieh, B.-C., Wang, W.-H., Hsieh, C.-C., et al. 2012, *ApJS*, 203, 23
- Ilbert, O., Salvato, M., Le Floch, E., et al. 2010, *ApJ*, 709, 644
- Karim, A., Schinnerer, E., Martínez-Sansigre, A., et al. 2011, *ApJ*, 730, 61
- Kashino, D., Silverman, J. D., Rodighiero, G., et al. 2013, *ApJL*, 777, L8
- Kenicutt, R. C., & Evans, N. J. 2012, *ARA&A*, 50, 531
- Kenicutt, R. C., Jr. 1998, *ARA&A*, 36, 189
- Koekemoer, A. M., Faber, S. M., Ferguson, H. C., et al. 2011, *ApJS*, 197, 36
- Kravtsov, A. V., Berlind, A. A., Wechsler, R. H., et al. 2004, *ApJ*, 609, 35
- Kriek, M., van Dokkum, P. G., Labbé, I., et al. 2009, *ApJ*, 700, 221
- Kroupa, P. 2001, *MNRAS*, 322, 231
- Law, D. R., Steidel, C. C., Shapley, A. E., et al. 2012, *ApJ*, 745, 85
- Lee, J. C., Kennicutt, R. C., Funes, S. J., et al. 2007, *ApJ*, 671, L113
- Lee, J. C., Ly, C., Spitler, L., et al. 2012, *PASP*, 124, 782
- Leitherer, C., Schaerer, D., Goldader, J. D., et al. 1999, *ApJS*, 123, 3
- Lotz, J. M., Madau, P., Giavalisco, M., Primack, J., & Ferguson, H. C. 2006, *ApJ*, 636, 592
- Lotz, J. M., Primack, J., & Madau, P. 2004, *AJ*, 128, 163
- Ly, C., Lee, J. C., Dale, D. A., et al. 2011, *ApJ*, 726, 109
- Ly, C., Malkan, M. A., Kashikawa, N., et al. 2012, *ApJL*, 747, L16
- Maraston, C. 2005, *MNRAS*, 362, 799
- Matsuda, Y., Smail, I., Geach, J. E., et al. 2011, *MNRAS*, 416, 2041
- Moorwood, A. F. M., van der Werf, P. P., Cuby, J. G., & Oliva, E. 2000, *A&A*, 362, 9
- Noeske, K. G., Weiner, B. J., Faber, S. M., et al. 2007, *ApJL*, 660, L43
- Oke, J. B. 1974, *ApJS*, 27, 21
- Papovich, C., Dickinson, M., Giavalisco, M., Conselice, C. J., & Ferguson, H. C. 2005, *ApJ*, 631, 101
- Peng, Y. J., Lilly, S. J., Kovač, K., et al. 2010, *ApJ*, 721, 193
- Puget, P., Stadler, E., Doyon, R., et al. 2004, *Proc. SPIE*, 5492, 978
- Ravindranath, S., Giavalisco, M., Ferguson, H. C., et al. 2006, *ApJ*, 652, 963
- Reddy, N. A., Pettini, M., Steidel, C. C., et al. 2012, *ApJ*, 754, 25
- Reddy, N. A., & Steidel, C. C. 2009, *ApJ*, 692, 778
- Renzini, A. 2006, *ARA&A*, 44, 141
- Retzlaff, J., Rosati, P., Dickinson, M., et al. 2010, *A&A*, 511, A50
- Rix, H.-W., Barden, M., Beckwith, S. V. W., et al. 2004, *ApJS*, 152, 163
- Schechter, P. 1976, *ApJ*, 203, 297
- Sedgwick, C., Serjeant, S., Pearson, C., et al. 2013, *MNRAS*, 436, 395
- Shapley, A. E. 2011, *ARA&A*, 49, 525
- Sobral, D., Best, P. N., Matsuda, Y., et al. 2012, *MNRAS*, 420, 1926
- Sobral, D., Smail, I., Best, P. N., et al. 2013, *MNRAS*, 428, 1128
- Springel, V., & Hernquist, L. 2003, *MNRAS*, 339, 312
- Steidel, C. C., Adelberger, K. L., Giavalisco, M., Dickinson, M., & Pettini, M. 1999, *ApJ*, 519, 1
- Stott, J. P., Sobral, D., Smail, I., et al. 2013, *MNRAS*, 430, 1158
- Swinbank, A. M., Smail, I., Chapman, S. C., et al. 2004, *ApJ*, 617, 64
- van Dokkum, P. G., Brammer, G., Fumagalli, M., et al. 2011, *ApJL*, 743, L15
- Wang, W.-H., Cowie, L. L., Barger, A. J., Keenan, R. C., & Ting, H.-C. 2010, *ApJS*, 187, 251
- Wuyts, S., Förster Schreiber, N. M., Lutz, D., et al. 2011, *ApJ*, 738, 106
- Wuyts, S., Förster Schreiber, N. M., van der Wel, A., et al. 2011, *ApJ*, 742, 96
- Xue, Y. Q., Luo, B., Brandt, W. N., et al. 2011, *ApJS*, 195, 10
- Yan, L., McCarthy, P. J., Freudling, W., et al. 1999, *ApJ*, 519, L47
- Zheng, X. Z., Bell, E. F., Rix, H.-W., et al. 2006, *ApJ*, 640, 784
- Zheng, X. Z., Dole, H., Bell, E. F., et al. 2007, *ApJ*, 670, 301